

Gaia Data Release 2: first stellar parameters from Apsis

René Andrae¹, Morgan Fouesneau¹, Orlagh Creevey², Christophe Ordenovic², Nicolas Mary³, Alexandru Burlacu⁴, Laurence Chaoul⁵, Anne Jean-Antoine-Piccolo⁵, Georges Kordopatis², Andreas Korn⁶, Yveline Lebreton^{7,8}, Chantal Panem⁵, Bernard Pichon², Frederic Thévenin², Gavin Walmsley⁵, Coryn A.L. Bailer-Jones^{1*}

¹ Max Planck Institute for Astronomy, Königstuhl 17, 69117 Heidelberg, Germany

² Université Côte d’Azur, Observatoire de la Côte d’Azur, CNRS, Laboratoire Lagrange, Bd de l’Observatoire, CS 34229, 06304 Nice cedex 4, France

³ Thales Services, 290 Allée du Lac, 31670 Labège, France

⁴ Telespazio France, 26 Avenue Jean-François Champollion, 31100 Toulouse, France

⁵ Centre National d’Etudes Spatiales, 18 av Edouard Belin, 31401 Toulouse, France

⁶ Division of Astronomy and Space Physics, Department of Physics and Astronomy, Uppsala University, Box 516, 75120 Uppsala, Sweden

⁷ LESIA, Observatoire de Paris, PSL Research University, CNRS UMR 8109, Université Pierre et Marie Curie, Université Paris Diderot, 5 place Jules Janssen, 92190 Meudon

⁸ Institut de Physique de Rennes, Université de Rennes 1, CNRS UMR 6251, F-35042 Rennes, France

Submitted to A&A 21 December 2017. Resubmitted 3 March 2018 and 3 April 2018. Accepted 3 April 2018

ABSTRACT

The second Gaia data release (Gaia DR2) contains, beyond the astrometry, three-band photometry for 1.38 billion sources. One band is the G band, the other two were obtained by integrating the Gaia prism spectra (BP and RP). We have used these three broad photometric bands to infer stellar effective temperatures, T_{eff} , for all sources brighter than $G = 17$ mag with T_{eff} in the range 3 000–10 000 K (some 161 million sources). Using in addition the parallaxes, we infer the line-of-sight extinction, A_G , and the reddening, $E(\text{BP} - \text{RP})$, for 88 million sources. Together with a bolometric correction we derive luminosity and radius for 77 million sources. These quantities as well as their estimated uncertainties are part of Gaia DR2. Here we describe the procedures by which these quantities were obtained, including the underlying assumptions, comparison with literature estimates, and the limitations of our results. Typical accuracies are of order 324 K (T_{eff}), 0.46 mag (A_G), 0.23 mag ($E(\text{BP} - \text{RP})$), 15% (luminosity), and 10% (radius). Being based on only a small number of observable quantities and limited training data, our results are necessarily subject to some extreme assumptions that can lead to strong systematics in some cases (not included in the aforementioned accuracy estimates). One aspect is the non-negativity constraint of our estimates, in particular extinction, which we discuss. Yet in several regions of parameter space our results show very good performance, for example for red clump stars and solar analogues. Large uncertainties render the extinctions less useful at the individual star level, but they show good performance for ensemble estimates. We identify regimes in which our parameters should and should not be used and we define a “clean” sample. Despite the limitations, this is the largest catalogue of uniformly-inferred stellar parameters to date. More precise and detailed astrophysical parameters based on the full BP/RP spectrophotometry are planned as part of the third Gaia data release.

Key words. methods: data analysis – methods: statistical – stars: fundamental parameters – surveys: Gaia

1. Introduction

The main objective of ESA’s Gaia satellite is to understand the structure, formation, and evolution of our Galaxy from a detailed study of its constituent stars. Gaia’s main technological advance is the accurate determination of parallaxes and proper motions for over one billion stars. Yet the resulting three-dimensional maps and velocity distributions which can be derived from these are of limited value if the physical properties of the stars remain unknown. For this reason Gaia is equipped with both a low-resolution prism spectrophotometer (BP/RP) operating over the entire optical range, and a high-resolution spectrograph (RVS) observing from 845–872 nm (the payload is described in Gaia Collaboration et al. 2016).

The second Gaia data release (Gaia DR2, Gaia Collaboration et al. 2018b) contains a total of 1.69 billion sources with posi-

tions and G-band photometry based on 22 months of mission observations. Of these, 1.33 billion sources also have parallaxes and proper motions (Lindgren et al. 2018). Unlike in the first release, Gaia DR2 also includes the integrated fluxes from the BP and RP spectrophotometers. These prism-based instruments produce low resolution optical spectrophotometry in the blue and red parts of the spectra which will be used to estimate astrophysical parameters for stars, quasars, and unresolved galaxies using the Apsis data processing pipeline (see Bailer-Jones et al. 2013). They are also used in the chromatic calibration of the astrometry. The processing and calibration of the full spectra is ongoing, and for this reason only their integrated fluxes, expressed as the two magnitudes G_{BP} and G_{RP} , are released as part of Gaia DR2 (see Fig. 1). The production and calibration of these data are described in Riello et al. (2018). 1.38 billion sources in Gaia DR2 have integrated photometry in all three bands, G , G_{BP} ,

* corresponding author, calj@mpia.de

and G_{RP} (Evans et al. 2018), and 1.23 billion sources have both five-parameter astrometry and three-band photometry.

In this paper we describe how we use the Gaia three-band photometry and parallaxes, together with various training data sets, to estimate the effective temperature T_{eff} , line-of-sight extinction A_G and reddening $E(\text{BP} - \text{RP})$, luminosity \mathcal{L} , and radius \mathcal{R} , of up to 162 million stars brighter than $G=17$ mag (some of these results are subsequently filtered out of the catalogue). We only process sources for which all three photometric bands are available. This therefore excludes the so-called bronze sources (Riello et al. 2018). Although photometry for fainter sources is available in Gaia DR2, we chose to limit our analysis to brighter sources on the grounds that, at this stage in the mission and processing, only these give sufficient photometric and parallax precision to obtain reliable astrophysical parameters. The choice of $G=17$ mag was somewhat arbitrary, however.¹ The work described here was carried out under the auspices of the Gaia Data Processing and Analysis Consortium (DPAC) within Coordination Unit 8 (CU8) (see Gaia Collaboration et al. 2016 for an overview of the DPAC). We realise that more precise, and possibly more accurate, estimates of the stellar parameters could be made by cross-matching Gaia with other survey data, such as GALEX (Morrissey et al. 2007), PanSTARRS (Chambers et al. 2016), and WISE (Cutri et al. 2014). However, the remit of the Gaia-DPAC is to process the Gaia data. Further exploitation, by including data from other catalogues, for example, is left to the community at large. We nonetheless hope that the provision of these “Gaia-only” stellar parameters will assist the exploitation of Gaia DR2 and the validation of such extended analyses.

We continue this article in section 2 with an overview of our approach and its underlying assumptions. This is followed by a description of the algorithm – called Priam – used to infer T_{eff} , A_G , and $E(\text{BP} - \text{RP})$ in section 3, and a description of the derivation of \mathcal{L} and \mathcal{R} – with the algorithm FLAME – in section 4. The results and the content of the catalogue are presented in section 5. More details on the catalogue itself (data fields etc.) can be found in the online documentation accompanying the data release. In section 6 we validate our results, in particular via comparison with other determinations in the literature. In section 7 we discuss the use of the data, focusing on some selections which can be used to identify certain types of stars, as well as the limitations of our results. *This is mandatory reading for anyone using the catalogue.* Priam and FLAME are part of a larger astrophysical parameter inference system in the Gaia data processing (Apsis). Most of the algorithms in Apsis have not been activated for Gaia DR2. (Priam itself is part of the GSP-Phot software package, which uses several algorithms to estimate stellar parameters.) We look ahead in section 8 to the improvements and extensions of our results which can be expected in Gaia DR3. We summarize our work in section 9. We draw attention to appendix B, where we define a “clean” subsample of our T_{eff} results.

In this article we will present both the estimates of a quantity and the estimates of its uncertainty, and we will also compare the estimated quantity with values in the literature. The term *uncertainty* refers to our computed estimate of how precise our estimated quantity is. This is colloquially (and misleadingly) called an “error bar”. We provide asymmetric uncertainties in the form of two percentiles from a distribution (upper and lower). We use the term *error* to refer to the difference between an estimated quantity and its literature estimate, whereby this difference could

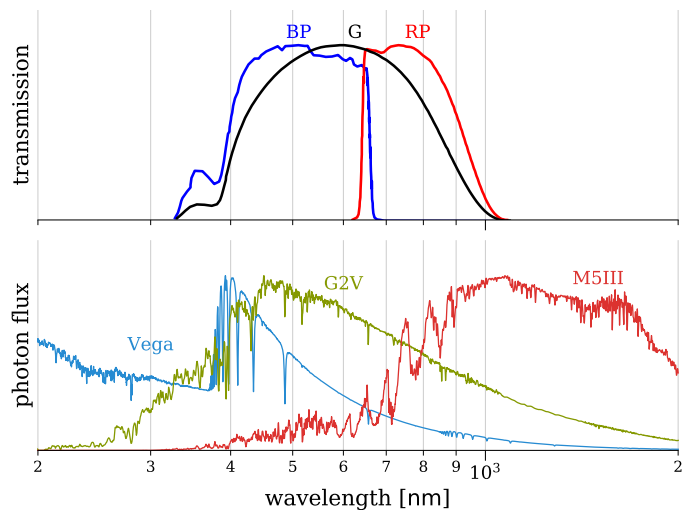


Fig. 1. The nominal transmissions of the three Gaia passbands (Jordi et al. 2010; de Bruijne 2012) compared with spectra of typical stars: Vega (A0V), a G2V star (Sun-like star), and an M5III star. Spectral templates from Pickles (1998). All curves are normalized to have the same maximum.

arise from a mistake in our estimate, in the literature value, or in both.

2. Approach and assumptions

2.1. Overview of procedure

We estimate stellar parameters source-by-source, using only the three Gaia photometric bands (for T_{eff}) and additionally the parallax (for the other four parameters). We do not use any non-Gaia data on the individual sources, and we do not make use of any global Galactic information, such as an extinction map or kinematics.

The three broad photometric bands – one of which is near degenerate with the sum of the other two (see Fig. 1) – provide relatively little information for deriving the intrinsic properties of the observed Gaia targets. They are not sufficient to determine whether the target is really a star as opposed to a quasar or an unresolved galaxy, for example. According to our earlier simulations, this will ultimately be possible using the full BP/RP spectra (using the Discrete Source Classifier in Apsis). As we are only working with sources down to $G=17$, it is reasonable to suppose that most of them are Galactic. Some will, inevitably, be physical binaries in which the secondary is bright enough to affect the observed signal. We nonetheless proceed as though all targets were single stars. Some binarity can be identified in the future using the composite spectrum (e.g. with the Multiple Star Classifier in Apsis) or the astrometry, both of which are planned for Gaia DR3.

Unsurprisingly, T_{eff} is heavily degenerate with A_G in the Gaia colours (see Fig. 2), so it seems near impossible that both quantities could be estimated from only colours. Our experiments confirm this. We work around this by estimating T_{eff} from the colours on the assumption that the star has (ideally) zero extinction. For this we use an empirically-trained machine learning algorithm (nowadays sometimes referred to as “data driven”). That is, the training data are observed Gaia photometry of targets which have had their T_{eff} estimated from other sources (generally

¹ The original selection was $G \leq 17$ mag, but due to a later change in the zeropoint, our final selection is actually $G \leq 17.068766$ mag.

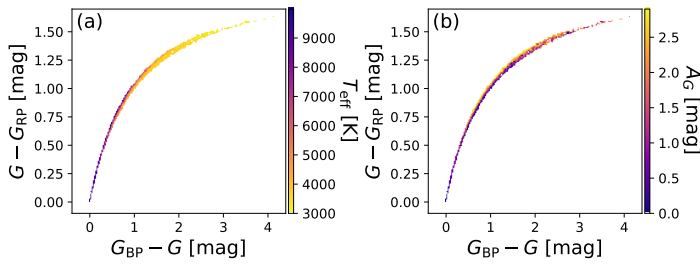


Fig. 2. Colour–colour diagrams for stars from the PARSEC 1.2S models with an extinction law from Cardelli et al. (1989) and $[\text{Fe}/\text{H}] = 0$. Both panels use the same data, spanning $A_0 = 0\text{--}4$ mag. We see that while T_{eff} is the dominant factor (panel a), it is strongly degenerate with extinction (panel b).

Table 1. The photometric zeropoints used to convert fluxes to magnitudes via Eq. 1 (Evans et al. 2018).

band	zeropoint (zp) [mag]
G	25.6884 ± 0.0018
G_{BP}	25.3514 ± 0.0014
G_{RP}	24.7619 ± 0.0020

spectroscopy). This training data set only includes stars which are believed to have low extinctions.

We separately estimate the interstellar absorption using the three bands together with the parallax, again using a machine learning algorithm. By using the magnitudes and the parallax, rather than the colours, the available signal is primarily the dimming of the sources due to absorption (as opposed to just the reddening). For this we train on synthetic stellar spectra, because there are too few stars with reliably estimated extinctions which could be used as an empirical training set. Note that the absorption we estimate is the extinction in the G-band, A_G , which is not the same as the (monochromatic) extinction parameter, A_0 . The latter depends only on the amount of absorption in the interstellar medium, whereas the former depends also on the spectral energy distribution (SED) of the star (see section 2.2 of Bailer-Jones 2011).² Thus even with fixed R_0 there is not a one-to-one relationship between A_0 and A_G . For this reason we use a separate model to estimate the reddening $E(\text{BP} - \text{RP})$, even though the available signal is still primarily the dimming due to absorption. By providing estimates of both absorption and reddening explicitly, it is possible to produce a de-reddened and de-extincted colour–magnitude diagram.

The inputs for our processing are fluxes, f , provided by the upstream processing (Riello et al. 2018). We convert these to magnitudes, m , using

$$m = -2.5 \log_{10} f + zp \quad (1)$$

where zp is the zeropoint listed in Table 1. All of our results except T_{eff} depend on these zeropoints.

We estimate the absolute G-band magnitude via the usual equation

$$M_G = G - 5 \log_{10} r + 5 - A_G. \quad (2)$$

² We distinguish between the V-band extinction A_V (which depends on the intrinsic source SED) and the monochromatic extinction A_0 at a wavelength of $\lambda = 547.7\text{nm}$ (which is a parameter of the extinction law and does not depend on the intrinsic source SED).

This is converted to a stellar luminosity using a bolometric correction (see section 4). The distance r to the target is taken simply to be the inverse of the parallax. Although this generally gives a biased estimate of the distance (Bailer-Jones 2015; Luri et al. 2018), the impact of this is mitigated by the fact that we only report luminosities when the fractional parallax uncertainty σ_ϖ/ϖ is less than 0.2. Thus, of the 161 million stars with T_{eff} estimates, only 77 million have luminosity estimates included in Gaia DR2.

Having inferred the luminosity and temperature, the stellar radius is then obtained by applying the Stefan–Boltzmann law

$$\mathcal{L} = 4\pi R^2 \sigma T_{\text{eff}}^4. \quad (3)$$

Because our *individual* extinction estimates are rather poor for most stars (discussed later), we chose not to use them in the derivation of luminosities, i.e. we set A_G to zero in equation 2. Consequently, while our temperature, luminosity, and radius estimates are self-consistent (within the limits of the adopted assumptions), they are formally inconsistent with our extinction and reddening estimates.

The final step is to filter out the most unreliable results: these do not appear in the catalogue (see appendix A). We furthermore recommend that for T_{eff} , only the “clean” subsample of our results be used. This is defined and identified using the flags in appendix B. When using extinctions, users may further want to make a cut to only retain stars with lower fractional parallax uncertainties.

2.2. Data processing

The software for Apsis is produced by teams in Heidelberg, Germany (Priam) and Nice, France (FLAME). The actual execution of the Apsis software on the Gaia data is done by the DPCC (Data Processing Centre CNES) in Toulouse, which also integrates the software. The processing comprises several operations, including the input and output of data and generation of logs and execution reports. The entire process is managed by a top-level software system called SAGA. Apsis is run in parallel on a multi-core Hadoop cluster system, with data stored in a distributed file system. The validation results are published on a web server (GaiaWeb) for download by the scientific software providers. The final Apsis processing for Gaia DR2 took place in October 2017. The complete set of sources (1.69 billion with photometry) covering all Gaia magnitudes was ingested into the system. From this the 164 million sources brighter than $G=17$ mag were identified and processed. This was done on 1000 cores (with 6 GB RAM per core), and ran in about 5000 hours of CPU time (around five hours wall clock time). The full Apsis system, which involves much more CPU-intensive processes, higher-dimensional input data (spectra), and of order one billion sources, will require significantly more resources and time.

3. Priam

3.1. General comments

Once the dispersed BP/RP spectrophotometry are available, the GSP-Phot software will estimate a number of different stellar parameters for a range of stellar types (see Liu et al. 2012; Bailer-Jones et al. 2013). For Gaia DR2 we use only the Priam module within GSP-Phot to infer parameters using integrated photometry and parallax. All sources are processed even if they have corrupt photometry (see Fig. 4) or if the parallax is missing or

non-positive. Some results are flagged and others filtered from the catalogue (see appendix A).

Priam employs extremely randomised trees (Geurts et al. 2006, hereafter EXTRA TREES), a machine learning algorithm with a univariate output. We use an ensemble of 201 trees and take the median of their outputs as our parameter estimate.³ We use the 16th and 84th percentiles of the EXTRA TREES ensemble as two uncertainty estimates; together they form a central 68% confidence interval. Note that this is, in general, asymmetric with respect to the parameter estimate. 201 trees is not very many from which to accurately compute such intervals – a limit imposed by available computer memory – but our validation shows them to be reasonable. EXTRA TREES are incapable of extrapolation: they cannot produce estimates or confidence intervals outside the range of the target variable (e.g. T_{eff}) in the training data. We experimented with other machine learning algorithms, such as support vector machine (SVM) regression (e.g. Deng et al. 2012) and Gaussian processes (e.g. Bishop 2006), but we found EXTRA TREES to be much faster (when training is also considered), avoid the high sensitivity of SVM tuning, and yet still provide results which are as good as any other method tried.

3.2. Effective temperatures

Given the observed photometry G , G_{BP} , and G_{RP} , we use the distance-independent colours $G_{\text{BP}} - G$ and $G - G_{\text{RP}}$ as the inputs to EXTRA TREES to estimate the stellar effective temperature T_{eff} . These two colours exhibit a monotonic trend with T_{eff} (Fig. 3). It is possible to form a third colour, $G_{\text{BP}} - G_{\text{RP}}$, but this is not independent, plus it is noisier since it does not contain the higher signal-to-noise ratio G -band. We do not propagate the flux uncertainties through EXTRA TREES. Furthermore, the integrated photometry is calibrated with two different procedures, producing so-called “gold-standard” and “silver-standard” photometry (Riello et al. 2018). As shown in Fig. 3, gold and silver photometry provide the same colour-temperature relations, thus validating the consistency of the two calibration procedures of Riello et al. (2018).

Since the in-flight instrument differs from its nominal pre-launch prescription (Jordi et al. 2010; de Bruijne 2012), in particular regarding the passbands (see Fig. 1), we chose not to train EXTRA TREES on synthetic photometry for T_{eff} . Even though the differences between nominal and real passbands are probably only of the order of ~ 0.1 mag or less in the zeropoint magnitudes (and thus even less in colours), we obtained poor T_{eff} estimates, with differences of around 800 K compared to literature values when using synthetic colours from the nominal passbands. We instead train EXTRA TREES on Gaia sources with observed photometry and T_{eff} labels taken from various catalogues in the literature. These catalogues use a range of data and methods to estimate T_{eff} : APOGEE (Alam et al. 2015) uses mid-resolution, near-infrared spectroscopy; the Kepler Input Catalogue⁴ (Huber et al. 2014) uses photometry; LAMOST (Luo et al. 2015) uses low-resolution optical spectroscopy; RAVE (Kordopatis et al. 2013) uses mid-resolution spectroscopy in a narrow window around the CaII triplet. The RVS auxiliary catalogue (Soubiran et al. 2014; Sartoretti et al. 2018), which we also use, is itself is a compilation of smaller catalogues, each again using different methods and different data. By combining all these different cat-

Table 2. Catalogues used for training EXTRA TREES for T_{eff} estimation showing the number of stars in the range from 3 000K to 10 000K that we selected and the mean T_{eff} uncertainty quoted by the catalogues.

catalogue	number of stars	mean T_{eff} uncertainty [K]
APOGEE	5 978	92
Kepler Input Catalogue	14 104	141
LAMOST	5 540	55
RAVE	2 427	61
RVS Auxiliary Catalogue	4 553	122
combined	32 602	102

alogues we are deliberately “averaging” over the systematic differences in their T_{eff} estimates. The validation results presented in sections 5 and 6 will show that this is not the limiting factor in our performance, however. This data set only includes stars which have low extinctions (although not as low as we would have liked). 95% of the literature estimates for these stars are below 0.705 mag for A_V and 0.307 mag for $E(B - V)$. (50% are below 0.335 mag and 0.13 mag respectively.) These limits exclude the APOGEE part of the training set, for which no estimates of A_V or $E(B - V)$ are provided. While APOGEE giants in particular can reach very high extinctions, they are too few to enable EXTRA TREES to learn to disentangle the effects of temperature and extinction in the training process. The training set is mostly near-solar metallicity stars: 95% of the stars have $[\text{Fe}/\text{H}] > -0.82$ and 99% have $[\text{Fe}/\text{H}] > -1.89$.

We compute our magnitudes from the fluxes provided by the upstream processing using equation 1. The values of the zero-points used here are unimportant, however, because the same zero-points are used for both training and application data.

We only retain stars for training if the catalogue specifies a T_{eff} uncertainty of less than 200K, and if the catalogue provides estimates of $\log g$ and $[\text{Fe}/\text{H}]$. The resulting set of 65 000 stars, which we refer to as the *reference sample*, is shown in Figs. 3 and 4. We split this sample into near-equal-sized training and test sets. To make this split reproducible, we use the digit sum of the Gaia source ID (a long integer which is always even): sources with even digit sums are used for training, those with odd for testing. The temperature distribution of the training set is shown in Fig. 5 (that for the test set is virtually identical). The distribution is very inhomogeneous. The impact of this on the results is discussed in section 5.2. Our supervised learning approach implicitly assumes that the adopted training distribution is representative of the actual temperature distribution all over the sky, which is certainly not the case (APOGEE and LAMOST probe quite different stellar populations, for example). However, such an assumption – that the adopted models are representative of the test data – can hardly be avoided. We minimise its impact by combining many different literature catalogues covering as much of the expected parameter space as possible.

Table 2 lists the number of stars (in the training set) from each catalogue, along with their typical T_{eff} uncertainty estimates as provided by that catalogue (which we will use in section 5.1 to infer the intrinsic temperature error of Priam).⁵ Mixing catalogues which have had T_{eff} estimated by different methods is likely to increase the scatter (variance) in our results, but

³ Further EXTRA TREES regression parameters are $k = 2$ random trials per split and $n_{\text{min}} = 5$ minimal stars per leaf node.

⁴ https://archive.stsci.edu/pub/kepler/catalogs/kic_ct_join_12142009.txt.gz

⁵ The subsets in Table 2 are so small that there are no overlaps between the different catalogues. Also note that the uncertainty estimates provided in the literature are sometimes clearly too small, e.g. for LAMOST.

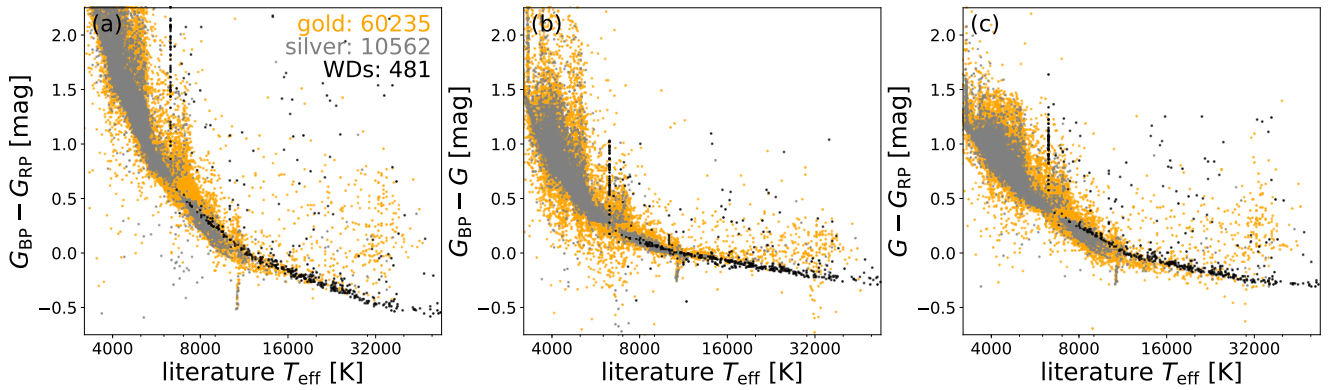


Fig. 3. Colour–temperature relations for Gaia data (our reference sample described in sect. 3.2) with literature estimates of T_{eff} . Each panel shows a different Gaia colour. Sources with gold-standard photometry are shown in orange and those with silver-standard photometry are shown in grey. White dwarfs matched to Kleinman et al. (2013) are shown in black.

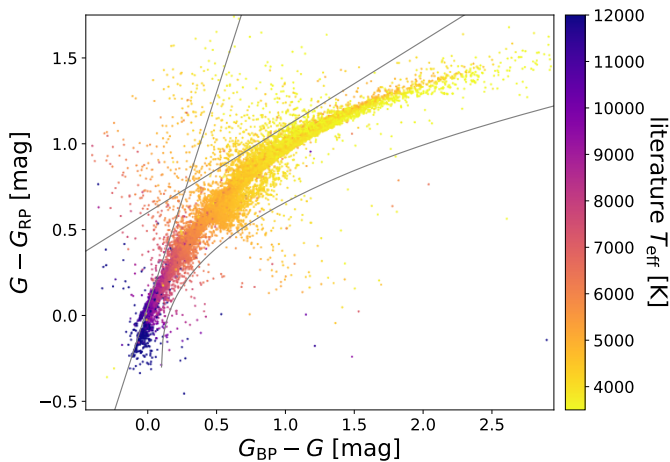


Fig. 4. Colour–colour diagram for Gaia data (our reference sample described in sect. 3.2) with literature estimates of T_{eff} . Grey lines show quality cuts where bad photometry is flagged (see Table B.1). Sources with excess flux larger than 5 have been discarded.

it is a property of EXTRATREES that this averaging should correspondingly reduce the bias in our results. Such a mixture is necessary, because no single catalogue covers all physical parameter space with a sufficiently large number of stars for adequate training. Even with this mix of catalogues we had to restrict the temperature range to 3000K–10 000K, since there are too few literature estimates outside of this range to enable us to get good results. For instance, there are only a few hundred OB stars with published T_{eff} estimates (Ramírez-Agudelo et al. 2017; Simón-Díaz et al. 2017). We tried to extend the upper temperature limit by training on white dwarfs with T_{eff} estimates from Kleinman et al. (2013), but as Fig. 3 reveals, the colour–temperature relations of white dwarfs (black points) differ significantly from those of OB stars (orange points with $T_{\text{eff}} \gtrsim 15\,000\text{K}$). Since EXTRATREES cannot extrapolate, this implies that stars with true $T_{\text{eff}} < 3000\text{K}$ or $T_{\text{eff}} > 10\,000\text{K}$ are “thrown back” into the interval 3000K–10 000K (see section 6.3). This may generate peculiar patterns when, for example, plotting a Hertzsprung–Russell diagram (see section 5.2).

The colour–colour diagram shown in Fig. 4 exhibits substantially larger scatter than expected from the PARSEC models shown in Fig. 2, even inside the selected good-quality region.

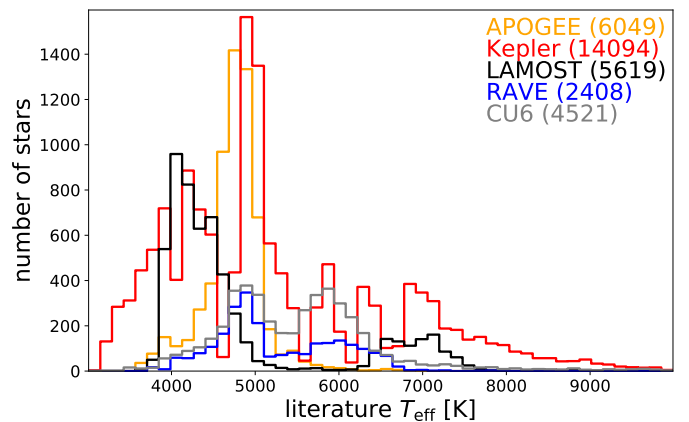


Fig. 5. Distribution of literature estimates of T_{eff} for the selected training sample. The numbers in parenthesis indicate how many stars from each catalogue have been used. The test sample distribution is almost identical.

This is not due to the measurement errors on fluxes, as the formal uncertainties in Fig. 4 are smaller than dot size for 99% of the stars plotted. Instead, this larger scatter reflects a genuine astrophysical diversity that is not accounted for in the models (for example due to metallicity variations, whereas Fig. 2 is restricted to $[\text{Fe}/\text{H}] = 0$).

3.3. Line-of-sight extinctions

For the first time, Gaia DR2 provides a colour–magnitude diagram for hundreds of millions of stars with good parallaxes. We complement this with estimates of the G -band extinction A_G and the $E(\text{BP} - \text{RP})$ reddening such that a dust-corrected colour–magnitude diagram can be produced.

As expected, we were unable to estimate the line-of-sight extinction from just the colours, since the colour is strongly influenced by T_{eff} (Fig. 2a vs. b). We therefore use the parallax ϖ to estimate the distance and then use equation (2) to compute $M_X + A_X$ for all three bands (which isn’t directly measured, but for convenience we refer to it from now on as an observable). We then use the three observables $M_G + A_G$, $M_{\text{BP}} + A_{\text{BP}}$, $M_{\text{RP}} + A_{\text{RP}}$ as features for training EXTRATREES. As shown in Fig. 6b, there is a clear extinction trend in this observable space, whereas the

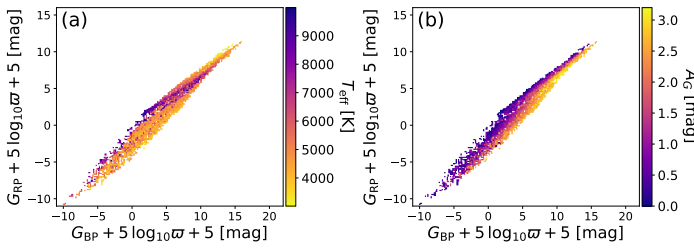


Fig. 6. Predicted relations between observables $G_{BP} + 5 \log_{10} w + 5 = M_{BP} + A_{BP}$ and $G_{RP} + 5 \log_{10} w + 5 = M_{RP} + A_{RP}$ using synthetic photometry including extinction.

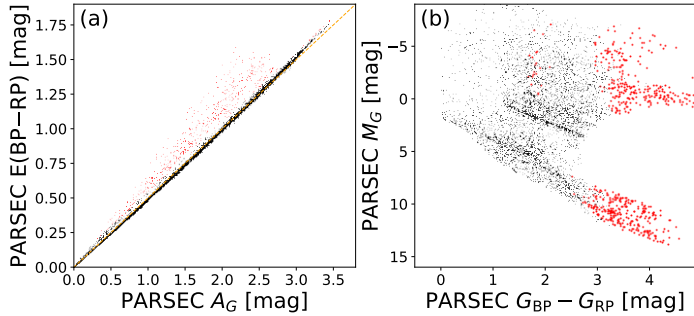


Fig. 7. Approximate relation between A_G and $E(BP-RP)$ (labels of EXTRA TREES training data) for PARSEC 1.2S models (Bressan et al. 2012) with $0 \leq A_G \leq 4$ and $3000 \text{ K} \leq T_{\text{eff}} \leq 10\,000 \text{ K}$. PARSEC models use the extinction law of Cardelli et al. (1989). We see in panel (a) that most stars follow the relation $A_G \sim 2 \cdot E(BP-RP)$ (dashed orange line) while the stars highlighted in red behave differently. Panel (b) shows that these stars with different A_G - $E(BP-RP)$ relation are very red (i.e. cool) sources.

dependence on T_{eff} (Fig. 6a) is much less pronounced than in colour-colour space (Fig. 2a). Yet, extinction and temperature are still very degenerate in some parts of the parameter space, and also there is no unique mapping of $M_X + A_X$ to extinction thus leading to further degeneracies (see section 6.5). Dependence on the parallax here restricts us to stars with precise parallaxes, but we want to estimate A_G and $E(BP-RP)$ in order to correct the colour-magnitude diagram (CMD), which itself is already limited by parallax precision. We do not propagate the flux and parallax uncertainties through EXTRA TREES.⁶

In order to estimate extinction we cannot train our models on literature values, for two reasons. First, there are very few reliable literature estimate of the extinction. Second, published estimates are of A_V and/or $E(B-V)$ rather than A_G and $E(BP-RP)$. We therefore use the PARSEC 1.2S models⁷ to obtain integrated photometry from the synthetic Atlas 9 spectral libraries (Castelli & Kurucz 2003) and the nominal instrument passbands (Fig. 1). These models use the extinction law from Cardelli et al. (1989) and O'Donnell (1994) with a fixed relative extinction parameter, $R_0=3.1$. We constructed a model grid that spans $A_0 = 0-4$ mag, a temperature range of 2 500–20 000 K, a $\log g$ range of 1–6.5 dex, and a fixed solar metallicity ($Z_\odot = 0.0152$, $[\text{Fe}/\text{H}] = 0$). We chose solar metallicity for our models since we could not cover all metallicities and because we expect most stars in our sample

to have $[\text{Fe}/\text{H}] \sim 0$. The extinctions A_G , A_{BP} , A_{RP} and the reddening $E(BP-RP) = A_{BP} - A_{RP}$ are then computed for each star by subtracting from the extinguished magnitudes the unextinguished magnitudes (which are obtained for $A_0 = 0$ mag). We used the sampling of the PARSEC evolutionary models as is, without further rebalancing or interpolation. Since this sampling is optimised to catch the pace of stellar evolution with time, the underlying distribution of temperatures, masses, ages, and extinctions is not representative of the Gaia sample. Therefore, as for T_{eff} , this will have an impact on our extinction estimates. However, while the Gaia colours are highly sensitive to T_{eff} , the photometry alone hardly allows us to constrain extinction and reddening, such that we expect that artefacts from this mismatch of the distributions in training data and real data will be washed out by random noise.

We use two separate EXTRA TREES models, one for A_G and one for $E(BP-RP)$. The input observables are $M_G + A_G$, $M_{BP} + A_{BP}$, and $M_{RP} + A_{RP}$ in both cases. That is, we do not infer $E(BP-RP)$ from colour measurements. On account of the extinction law, $E(BP-RP)$ and A_G are strongly correlated to the relation $A_G \sim 2 \cdot E(BP-RP)$ over most of our adopted temperature range, as can be seen in Fig. 7.⁸ The finite scatter is due to the different spectral energy distributions of the stars: the largest deviations occur for very red sources. Note that because EXTRA TREES cannot extrapolate beyond the training data range, we avoid negative estimates of A_G and $E(BP-RP)$. This non-negativity means the likelihood cannot be Gaussian, and as discussed in appendix E, a truncated Gaussian is more appropriate.

Evidently, the mismatch between synthetic and real Gaia photometry, i.e. differences between passbands used in the training and the true passbands (and zeropoints), will have a detrimental impact on our extinction estimates, possibly leading to systematic errors. Nonetheless, this mismatch is only ~ 0.1 mag in the zeropoints (Evans et al. 2018) and as shown in Gaia Collaboration et al. (2018a), the synthetic photometry (using inflight passbands) of isochrone models actually agrees quite well with the Gaia data. Indeed, as will be shown in sections 5.2 and 6.6, this mismatch appears not to lead to obvious systematic errors.⁹

Although we cannot estimate temperatures from these models with our data, the adopted T_{eff} range of 2500–20 000 K for the PARSEC models allows us to obtain reliable extinction and reddening estimates for intrinsically very blue sources such as OB stars, even though the method described in section 3.2 cannot provide good T_{eff} estimates for them.

4. FLAME

The Final Luminosity, Age, and Mass Estimator (FLAME) module aims to infer fundamental parameters of stars. In Gaia DR2 we only activate the components for inferring luminosity and radius. Mass and age will follow in the next data release, once GSP-Phot is able to estimate $\log g$ and $[\text{Fe}/\text{H}]$ from the BP/RP spectra and the precision in T_{eff} and A_G improves. We calculate luminosity \mathcal{L} with

$$-2.5 \log_{10} \mathcal{L} = M_G + BC_G(T_{\text{eff}}) - M_{\text{bol}\odot} \quad (4)$$

where \mathcal{L} is in units of \mathcal{L}_\odot (Table 3), M_G is the absolute magnitude of the star in the G-band, $BC_G(T_{\text{eff}})$ is a temperature

⁶ We found that propagating the flux and parallax uncertainties through the EXTRA TREES has no noteworthy impact on our results, i.e. our extinction and reddening estimates are not limited by the expected precision of the input data.

⁷ <http://stev.oapd.inaf.it/cgi-bin/cmd>

⁸ Using different stellar atmosphere models with different underlying synthetic SEDs, Jordi et al. (2010) found a slightly different relation between A_G and $E(BP-RP)$.

⁹ The situation for T_{eff} would be different, where using synthetic colours results in large errors.

Table 3. Reference solar parameters.

quantity	unit	value
\mathcal{R}_\odot	m	$6.957e+08$
$T_{\text{eff}\odot}$	K	$5.772e+03$
\mathcal{L}_\odot	W	$3.828e+26$
$M_{\text{bol}\odot}$	mag	4.74
$BC_{G\odot}$	mag	+0.06
V_\odot	mag	-26.76
$BC_{V\odot}$	mag	-0.07
$M_{V\odot}$	mag	4.81

dependent bolometric correction (defined below), and $M_{\text{bol}\odot} = 4.74$ mag is the solar bolometric magnitude as defined in IAU Resolution 2015 B2¹⁰. The absolute magnitude is computed from the G-band flux and parallax using equations 1 and 2. As the estimates of extinction provided by Priam were shown not to be sufficiently accurate on a star-to-star basis for many of our brighter validation targets, we set A_G to zero when computing M_G . The radius \mathcal{R} is then calculated from equation 3 using this luminosity and T_{eff} from Priam. These derivations are somewhat trivial; at this stage FLAME simply provides easy access for the community to these fundamental parameters.

Should a user want to estimate luminosity or radius assuming a non-zero extinction $A_{G,\text{new}}$ and/or a change in the bolometric correction of ΔBC_G , one can use the following expressions

$$\mathcal{L}_{\text{new}} = \mathcal{L} 10^{0.4(A_{G,\text{new}} - \Delta BC_G)} \quad (5)$$

$$\mathcal{R}_{\text{new}} = \mathcal{R} 10^{0.2(A_{G,\text{new}} - \Delta BC_G)} \quad (6)$$

4.1. Bolometric Correction

We obtained the bolometric correction BC_G on a grid as a function of T_{eff} , $\log g$, $[\text{M}/\text{H}]$, and $[\alpha/\text{Fe}]$, derived from the MARCS synthetic stellar spectra (Gustafsson et al. 2008). The synthetic spectra cover a T_{eff} range from 2500 K to 8000 K, $\log g$ from -0.5 to 5.5 dex, $[\text{Fe}/\text{H}]$ from -5.0 to +1.0 dex, and $[\alpha/\text{Fe}]$ from +0.0 to +0.4 dex. Magnitudes are computed from the grid spectra using the G filter (Fig. 1). These models assume local thermodynamic equilibrium (LTE), with plane-parallel geometry for dwarfs and spherical symmetry for giants. We extended the T_{eff} range using the BC_G from Jordi et al. (2010), but with an offset added to achieve continuity with the MARCS models at 8000 K. However, following the validation of our results (discussed later), we choose to filter out FLAME results for stars with T_{eff} outside the range 3300 – 8000 K (see appendix A).

For the present work we had to address two issues. First, BC_G is a function of four stellar parameters, but it was necessary to project this to be a function of just T_{eff} , since for Gaia DR2 we do not yet have estimates of the other three stellar parameters. Second, the bolometric correction needs a reference point to set the absolute scale, as this is not defined by the models. We will refer to this as the *offset* of the bolometric correction, and it has been defined here so that the solar bolometric correction $BC_{G\odot}$ is +0.06 mag. Further details are provided in appendix D.

To provide a 1-D bolometric correction, we set $[\alpha/\text{Fe}] = 0$ and select the BC_G corresponding¹¹ to $|[\text{Fe}/\text{H}]| < 0.5$. As there is still a dependence on $\log g$, we adopt for each T_{eff} bin the mean value of the bolometric correction. We also compute the standard deviation $\sigma(BC_G)$ as a measure of the uncertainty due to the dispersion in $\log g$. We then fit a polynomial to these values to define the function

$$BC_G(T_{\text{eff}}) = \sum_{i=0}^4 a_i (T_{\text{eff}} - T_{\text{eff}\odot})^i \quad (7)$$

The values of the fitted coefficients are given in Table 4. The fit is actually done with the offset parameter a_0 fixed to $BC_{G\odot} = +0.06$ mag, the reference bolometric value of the Sun (see appendix D). We furthermore make two independent fits, one for the T_{eff} in the range 4000–8000 K and another for the range 3300–4000 K.

Table 4. Polynomial coefficients of the model $BC_G(T_{\text{eff}})$ defined in equation 7 (column labelled BC_G). A separate model was fit to the two temperature ranges. The coefficient a_0 was fixed to its value for the 4000–8000 K temperature range. For the lower temperature range a_0 was fixed to ensure continuity at 4000 K. The column labelled $\sigma(BC_G)$ lists the coefficients for a model of the uncertainty due to the scatter of $\log g$.

	BC_G	$\sigma(BC_G)$
4000 – 8000 K		
a_0	6.000e-02	2.634e-02
a_1	6.731e-05	2.438e-05
a_2	-6.647e-08	-1.129e-09
a_3	2.859e-11	-6.722e-12
a_4	-7.197e-15	1.635e-15
3300 – 4000 K		
a_0	1.749e+00	-2.487e+00
a_1	1.977e-03	-1.876e-03
a_2	3.737e-07	2.128e-07
a_3	-8.966e-11	3.807e-10
a_4	-4.183e-14	6.570e-14

Fig. 8 shows BC_G as a function of T_{eff} . The largest uncertainty is found for $T_{\text{eff}} < 4000$ K where the spread in the values can reach up to ± 0.3 mag, due to not distinguishing between giants and dwarfs¹². We estimated the uncertainty in the bolometric correction by modelling the scatter due to $\log g$ as a function of T_{eff} , using the same polynomial model as in equation 7. The coefficients for this model are also listed in Table 4.

4.2. Uncertainty estimates on luminosity and radius

The upper and lower uncertainty levels for \mathcal{L} are defined symmetrically as $\mathcal{L} \pm \sigma$, where σ has been calculated using a standard (first order) propagation of the uncertainties in the G-band mag-

¹⁰ Choosing $|[\text{Fe}/\text{H}]| < 1.0$ or including $[\alpha/\text{Fe}] = +0.4$ only changed the BC_G in the third decimal place, well below its final uncertainty. Fixing $[\text{Fe}/\text{H}]$ to a single value (e.g. zero) had just as little impact relative to the uncertainty.

¹² We could have estimated a mass from luminosities and colours in order to estimate $\log g$, and subsequently iterated to derive new luminosities and radii. However, given the uncertainties in our stellar parameters, we decided against doing this.

¹⁰ https://www.iau.org/static/resolutions/IAU2015_English.pdf

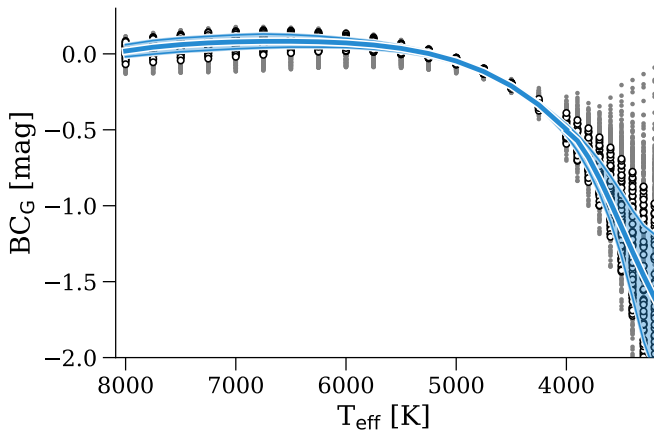


Fig. 8. Bolometric corrections from the MARCS models (grey dots) and the subset we selected (open circles) to fit the polynomial model (equation 7, with fixed a_0), to produce the thick blue line and the associated 1- σ uncertainty indicated by the blue shaded region.

nitude and parallax¹³. Note, however, that we do not include the additional uncertainty arising from the temperature which would propagate through the bolometric correction (equation 4). For \mathcal{R} , the upper and lower uncertainty levels correspond to the radius computed using the upper and lower uncertainty levels for T_{eff} . As these T_{eff} levels are 16th and 84th percentiles of a distribution, and percentiles are conserved under monotonic transformations of distributions, the resulting radius uncertainty levels are also the 16th and 84th percentiles. This transformation neglects the luminosity uncertainty, but in most cases the T_{eff} uncertainty dominates for the stars in the published catalogue (i.e. filtered results; see Appendix A). The distribution of the uncertainties in \mathcal{R} and \mathcal{L} for different parameter ranges are shown as histograms in Figs. 9. The radius uncertainty defined here is half the difference between the upper and lower uncertainty levels. It can be seen that the median uncertainties in \mathcal{L} , which considers just the uncertainties in G and ϖ , is around 15%. For radius it's typically less than 10%. While our uncertainty estimates are not particularly precise, they provide the user with some estimate of the quality of the parameter.

5. Results and catalogue content

We now present the Apsis results in Gaia DR2 by looking at the performance on various test data sets. We refer to summaries of the differences between our results and their literature values as “errors”, as by design our algorithms are trained to achieve minimum differences for the test data. This does not mean that the literature estimates are “true” in any absolute sense. We ignore here the inevitable inconsistencies in the literature values, since we do not expect our estimates to be good enough to be substantially limited by these.

¹³ A revision of the parallax uncertainties between processing and the data release means that our fractional luminosity uncertainties are incorrect by factors varying between 0.6 and 2 (for 90% of the stars), with some dependence on magnitude (see appendix A of Lindegren et al. (2018), in particular the upper panel of Figure A.2). Although there was no opportunity to rederive the luminosity uncertainties, these revised parallax uncertainties (i.e. those in Gaia DR2) were used when filtering the FLAME results according to the criterion in appendix A.

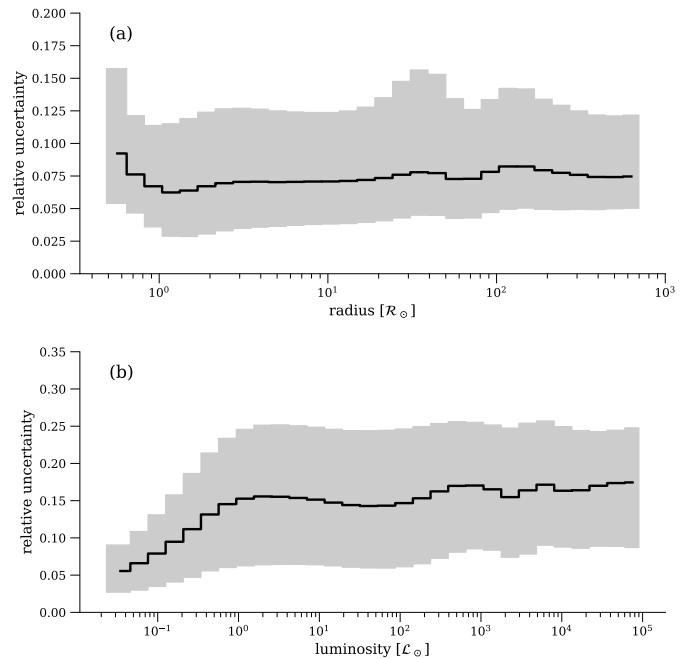


Fig. 9. Distribution of FLAME relative uncertainties for (a) radius and (b) luminosity, after applying the GDR2 filtering (Table A.1). In both panels the black line shows the median value of the uncertainty, and the shaded regions indicate the 16th and 84th percentiles.

5.1. Results for T_{eff}

We use the test data set (as defined in section 3.2) to examine the quality of our T_{eff} estimates. We limit our analyses to those 98% of sources which have “clean” Priam flags for T_{eff} (defined in appendix B). Our estimated values range from 3229 K to 9803 K on this test set. The smallest lower uncertainty level is 3098 K and the highest upper uncertainty level is 9985 K. As the uncertainties are percentiles of the distribution of EXTRA TREES outputs, and this algorithm cannot extrapolate, these are constrained to the range of our training data (which is 3030 K to 9990 K).

Table 5. T_{eff} error on various sets of test data for sources which were not used in training. We also show test results for 8599 sources with clean flags from the GALAH catalogue (Martell et al. 2017), a catalogue not used in training at all. The bias is the mean error.

reference catalogue	bias [K]	RMS error [K]
APOGEE	−105	383
Kepler Input Catalogue	−6	232
LAMOST	−9	381
RAVE	21	216
RVS Auxiliary Catalogue	−50	425
GALAH	−18	233

Fig. 10 compares our T_{eff} estimates with the literature estimates for our test data set. The root-mean-squared (RMS) test error is 324 K, which includes a bias (defined as the mean residual) of −29 K. For comparison, the RMS error on the training set is 217 K, with a bias of −22 K (better than the test set, as expected). We emphasise that the RMS test error of 324 K is an average value over the different catalogues, which could have different physical T_{eff} scales. Moreover, since our test sample, just like our training sample, is not representative for the general stellar population in Gaia DR2, the 324 K uncertainty estimate is

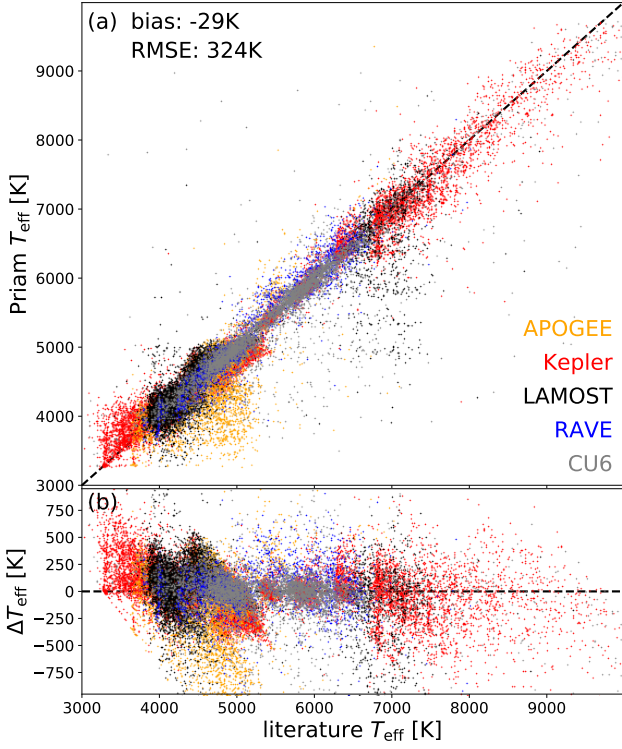


Fig. 10. Comparison of Priam T_{eff} estimates with literature values on the test data set for sources with clean flags, colour coded according to catalogue. The upper panel plots the Priam outputs; the lower panel plots the residuals $\Delta T_{\text{eff}} = T_{\text{eff}}^{\text{Priam}} - T_{\text{eff}}^{\text{literature}}$.

likely to be an underestimate. Nevertheless, given this RMS test error of 324 K, we can subtract (in quadrature) the 102 K literature uncertainty (Table 2) to obtain an internal test error estimate of 309 K for Priam.

Table 5 shows that the errors vary considerably for the different reference catalogues. Consequently, the temperature errors for a stellar population with a restricted range of T_{eff} could differ from our global estimates (see sections 6.3 and 6.4). This is illustrated in panels (a) and (b) of Fig. 11. If the estimated temperature is below about 4000 K, we can expect errors of up to 550 K. Likewise, if the estimated temperature is above 8000 K, the absolute error increases while the relative error is consistently below 10% for $T_{\text{eff}} \gtrsim 4000$ K. The dependence of test error on literature temperatures (Fig. 11c) shows the same behaviour. Note that the errors are dominated by outliers, since when we replace the mean by the median, the errors are much lower (solid vs. dashed lines in Fig. 11).

As we can see from Fig. 11d, the temperature error increases only very slightly with G magnitude, which is best seen in the medians since outliers can wash out this trend in the means. Fig. 11e shows that the temperature error is weakly correlated with the estimated A_G extinction, but now more dominant in the mean than the median. This is to be expected since our training data are mostly stars with low extinctions. Stars with high extinctions are under-represented, and due to the extinction–temperature degeneracy they are assigned systematically lower T_{eff} estimates. This is particularly apparent when we plot the temperature residuals in the Galactic coordinates (Fig. 12): stars in the Galactic plane, where extinctions are higher, have systematically negative residuals. Finally, Fig. 11f shows that the temperature error also depends on the $G_{\text{BP}} - G_{\text{RP}}$ colour of the star.

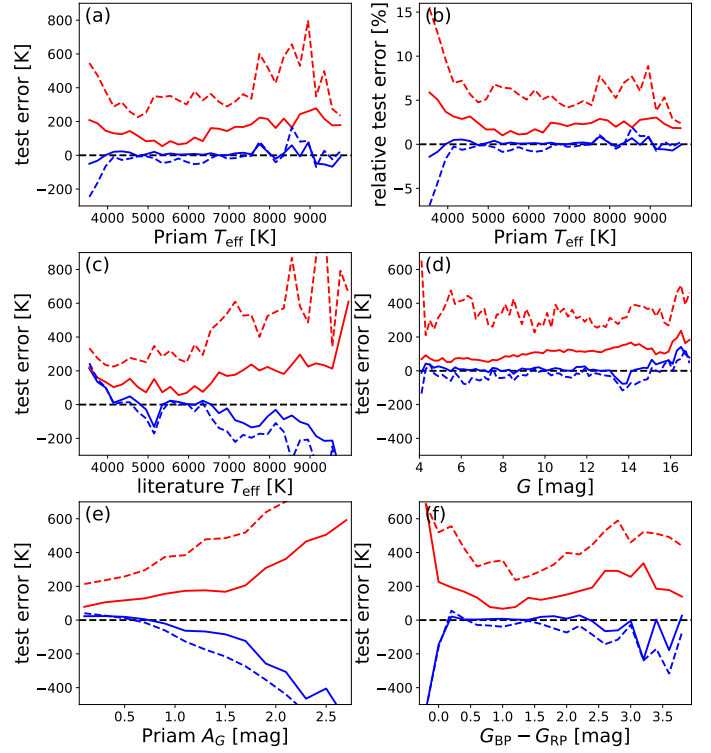


Fig. 11. Dependence of T_{eff} test errors on estimated T_{eff} (panel a and b), on literature T_{eff} (panel c), on G (panel d), estimated A_G (panel e) and $G_{\text{BP}} - G_{\text{RP}}$ colour (panel f). Red lines show root-mean-squared errors (dashed) and root-median-squared errors (solid). Blue lines show mean errors (dashed) and median errors (solid), as measures of bias.

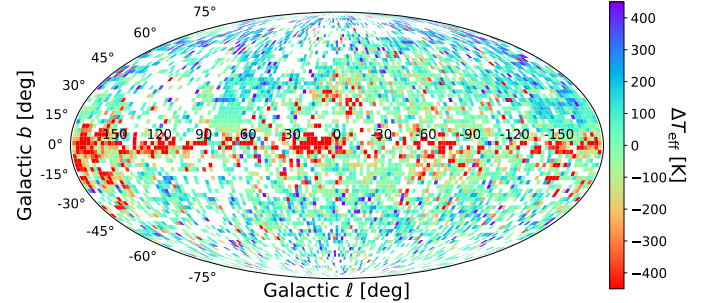


Fig. 12. Mean difference of Priam T_{eff} from literature values for test data, plotted in Galactic coordinates (Mollweide projection).

Very blue and very red stars were comparatively rare in the training data. For the bluest stars, we see that we systematically underestimate T_{eff} . This is a direct consequence of the upper limit of 10 000 K in the training sample (but not in the Galaxy) and the inability of EXTRA TREES to extrapolate.

Fig. 12 also suggests a slight tendency to systematically overestimate T_{eff} at high Galactic latitudes. Halo stars typically have subsolar metallicity, hence tend to be bluer for a given T_{eff} than solar metallicity stars. This may lead Priam, which is trained mostly on solar-metallicity stars, to overestimate T_{eff} (see Sect. 6.1). Alternatively, although the extinction in our empirical training sample is generally low, it is not zero, such that for high latitude stars with almost zero extinction, Priam would overes-

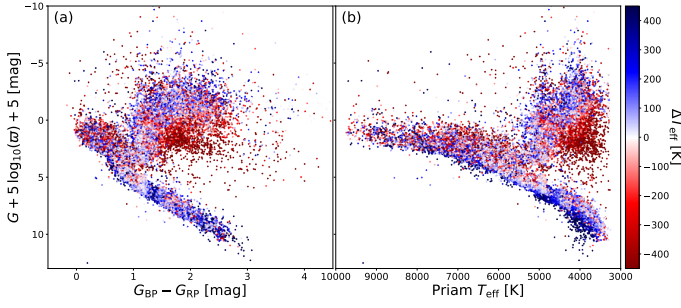


Fig. 13. Difference between Priam T_{eff} and literature values for the test data shown in a colour-magnitude diagram (left panel) and Hertzsprung-Russell diagram (right panel).

timate T_{eff} . Most likely, both effects are at work, with the latter presumably dominating.

The differences between our temperature estimates and the literature values are shown in a CMD in Fig. 13a. Priam predicts lower T_{eff} in those parts of the CMD where we suspect the extinction may be high (e.g. the lower part of the giant branch). Conversely, the overestimation of T_{eff} in the lower part of the main sequence may be due nearby faint stars having lower extinctions than the low but non-zero extinction in our empirical training sample. These systematics with extinction agree with Fig. 11e. This will be discussed further in the next section.

In order to assess our uncertainty estimates, we again use the test data. Ideally, the distribution of our uncertainty estimates should coincide with the distribution of the errors. We find that for 23% of test stars, their literature values are below our lower uncertainty levels (which are 16th percentiles), whereas for 22% of test stars the literature values are above our upper uncertainty levels (84th percentiles). One interpretation of this is that our uncertainty intervals are too narrow, i.e. that the supposed 68% central confidence interval (84th minus 16th) is in fact more like a 55% confidence interval. However, the literature estimates have finite errors, perhaps of order 100–200 K, and these will increase the width of the residual distribution (compared to computing residuals using perfect estimates). We investigate this more closely by plotting the distribution of residuals normalised by the combined (Priam and literature) uncertainty estimates. This is shown in Fig. 14 for all our test data and different directions in the Galaxy. If the combined uncertainties were Gaussian measures of the residuals, then the histograms should be Gaussian with zero mean and unit standard deviation (the red curves). This is generally the case, and suggests that, although we do not propagate the flux uncertainties, the Priam uncertainty estimates may indeed provide 68% confidence intervals and that the 55% obtained above arose only from neglecting literature uncertainties. The left column in Fig. 14 shows a systematic trend in the residuals (mean of the histogram) as a function of Galactic latitude, which is also evident from Fig. 12. This most likely reflects a systematic overestimation of T_{eff} for zero-extinction stars at high latitudes. Also note that the panels for $\ell = 60^\circ - 100^\circ$ and $|b| = 10^\circ - 20^\circ$ exhibit narrow peaks. These two panels are dominated by the Kepler field, which makes up 43% of the training sample (see Table 2). The fact that these two peaks are sharper than the unit Gaussian suggests overfitting of stars from the Kepler sample.¹⁴ Concerning the asymmetry of the conference in-

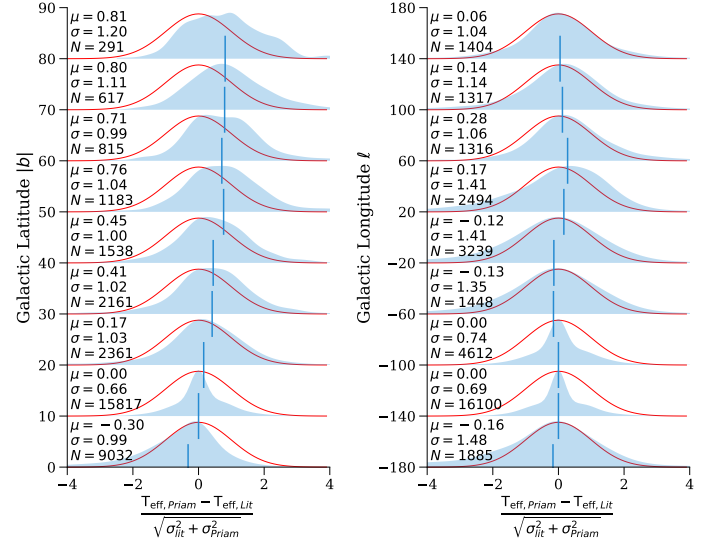


Fig. 14. Distribution of the T_{eff} residuals (Priam minus literature) normalized by their combined uncertainties for the test data set, for different Galactic latitudes (left column) and longitudes (right column). The Priam uncertainty σ_{Priam} used in the computation for each star is formed from the lower uncertainty level if $T_{\text{eff,Priam}} > T_{\text{eff,Lit}}$, and from the upper uncertainty level otherwise. The upper left corner of each panel reports the mean μ and standard deviation (σ) of these normalized residuals. The red curves are unit Gaussian distributions. The vertical lines indicate the median of each distribution. For unbiased estimates and correct uncertainties in both the literature and our work, the histograms and the red Gaussians should match.

tervals, we find that for 57% of sources, upper minus median and median minus lower differ by less than a factor of two, while for 2.5% of sources these two bands can differ by more than a factor of ten.

5.2. Results for A_G and $E(\text{BP} - \text{RP})$

We look now at our estimates of line-of-sight extinction A_G and reddening $E(\text{BP} - \text{RP})$. Where appropriate we will select on parallax uncertainty. As will be discussed in section 6.5, some of our estimates of A_G and $E(\text{BP} - \text{RP})$ suffered from strong degeneracies. These (about one third of the initial set of estimates) were filtered out of the final catalogue.

As explained in section 3.3, we are unable to estimate the line-of-sight extinction from just the colours. Fig. 15 demonstrates that neither A_G nor $E(\text{BP} - \text{RP})$ has a one-to-one relation with the colour. (Plots against the other two colours are shown in the online Gaia DR2 documentation.) This complex distribution is the combined result of having both very broad filters and a wide range of stellar types. It may be possible to find an approximate colour-extinction relation only if one can a priori restrict the sample to a narrow part of the HRD, such as giant stars.

In addition, using only three optical bands (and parallax), we do not expect very accurate extinction estimates. A direct comparison to the literature is complicated by the fact that the literature does not estimate A_G or $E(\text{BP} - \text{RP})$ but rather A_0 , A_V , or $E(B - V)$. We compare them nonetheless on a star-by-star basis in Table 6, and Fig. 16 shows the results for stars for the Kepler Input Catalog. The largest RMS difference for these samples is 0.34 mag between A_G and A_V and 0.24 mag between $E(\text{BP} - \text{RP})$ and $E(B - V)$. This appears to be dominated primarily by systematically larger values of A_G and $E(\text{BP} - \text{RP})$. The dif-

¹⁴ Propagating the flux errors through the EXTRA TREES gives slightly lower test errors (supporting the idea that we may overfit the Kepler sample) and brings the normalised residuals closer to a unit Gaussian.

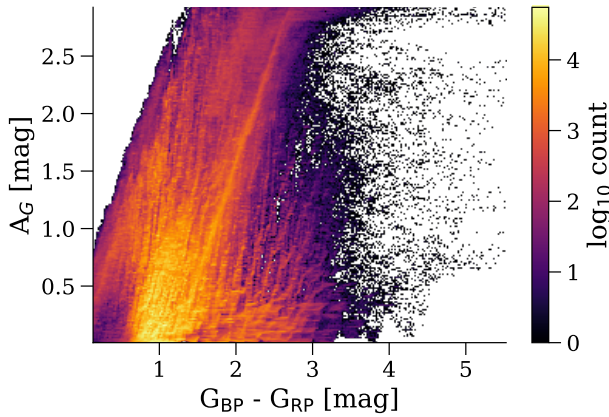


Fig. 15. Estimates of A_G versus source colours over the entire sky. While there is an expected overall trend of redder sources being more extinct, the very broad dispersion shows that $G_{BP} - G_{RP}$ is not a good proxy for extinction. Note that the saturation of the extinction arises from our model assumptions.

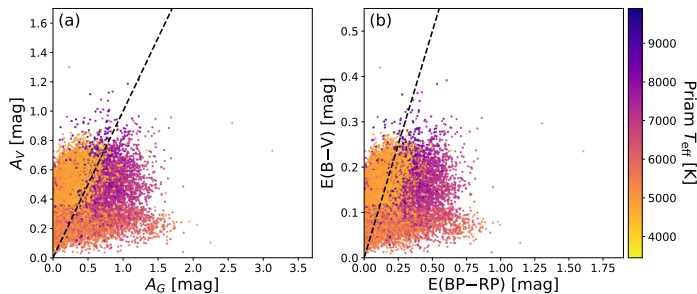


Fig. 16. A_G vs. A_V (panel a) and $E(BP-RP)$ vs. $E(B-V)$ (panel b) for 22 894 stars from the Kepler Input Catalog with parallax uncertainty less than 20%. The dashed line shows the identity relation. As discussed in the main text, this comparison is inconclusive since A_G and $E(BP-RP)$ are subject to large uncertainties but they cannot scatter into negative values (thus causing seeming biases). Furthermore, the Gaia passbands are very broad and thus strongly depend on the intrinsic source SED. Dashed lines indicate one-to-one relations.

ferences between nominal and real passbands are only of order 0.1 mag in the zeropoints (Evans et al. 2018) and thus are unlikely to explain this. Instead, these large values arise from the degeneracies in the extinction estimation (see section 6.5) and the non-trivial transformation between A_V and A_G and between $E(B-V)$ and $E(BP-RP)$. To mitigate this problem we validate A_G using red clump stars in section 6.6. For now, we conclude from Table 6 that the scatter in A_G may be as high as 0.34 mag and the scatter in $E(BP-RP)$ as high as 0.24 mag. Given such a large scatter, we can only verify the extinction estimates at an ensemble level. Let us also emphasise that since EXTRA TREES cannot produce negative results for A_G or $E(BP-RP)$, the large random scatter may give rise to an *apparent* systematic error¹⁵ that can also be seen in Fig. 16. We also find an approximate relation $A_G \sim 2 \cdot E(BP-RP)$ (Fig. 17). This is essentially by construction, as we use the same PARSEC models for the determination of both quantities (see Fig. 7).

Fig. 18 shows the distribution of T_{eff} vs. A_G for all stars with clean Priam flags. Since EXTRA TREES cannot extrapolate from the

Table 6. Comparison of our A_G and $E(BP-RP)$ estimates with literature values of A_V and $E(B-V)$ (for sources with $\sigma_\pi/\pi < 0.2$, but no selection on flags). In each case we quote the mean difference and the RMS difference.

		$A_G - A_V$		$E(BP-RP) - E(B-V)$
Kepler Input Catalog (15 143)	RMS	0.34mag		0.18mag
	mean	0.00mag		0.07mag
Lallement et al. (2014) (1431 stars)	RMS	–		0.24mag
	mean	–		0.16mag
Rodrigues et al. (2014) (1315 stars)	RMS	0.21mag		–
	mean	0.08mag		–

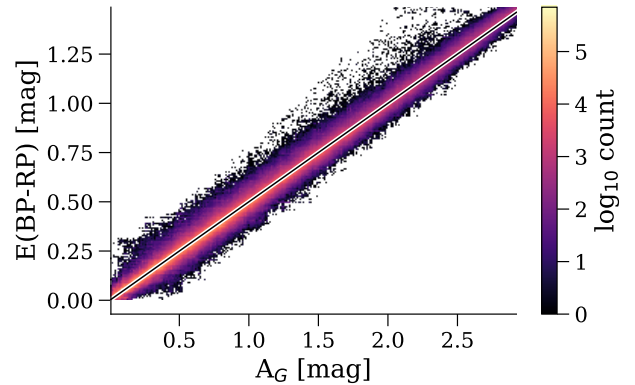


Fig. 17. A_G vs $E(BP-RP)$ for sources with $\sigma_\pi < 1$ mas (no selection on flags). The dash black line shows the approximation $A_G \sim 2 \cdot E(BP-RP)$.

T_{eff} training data range of 3000K–10 000K, the results are restricted to this range. We see unoccupied regions on this plot, labelled “A” and “B”. The empty region A is due to the apparent magnitude limit of $G \leq 17$, which removes stars with lower T_{eff} already at lower A_G , since they are fainter. This is expected. However, the second empty region labelled B in Fig. 18 is more interesting. There are seemingly no hot stars with high extinctions. This void is an artefact and is due to our EXTRA TREES training sample (for extinctions) comprising only low-extinction stars. Therefore, if hot stars in the overall sample are reddened by dust, they have no counterparts in the training sample and are thus assigned systematically lower temperatures which, given the T_{eff} training sample, is the only way that EXTRA TREES can match their reddish colours. We also note the vertical stripes in Fig. 18, which are a consequence of the inhomogeneous temperature distribution in our training sample (see Fig. 5). Unfortunately, a desirable rebalancing of our training sample fell victim to the tight processing schedule for Gaia DR2. However, these results are not our final data products and revised training sets will be used for Gaia DR3 (section 8).

Although our extinction estimates are inaccurate on a star-by-star level, our main goal in estimating A_G and $E(BP-RP)$ is to enable a dust correction of the observed CMD. To this end, it is sufficient if our extinction estimates are mostly unbiased such that they are applicable at the ensemble level. This is often the case, as is shown in Fig. 19. The observed CMD in Fig. 19a exhibits a very diffuse source distribution. In particular, the giant branch is completely washed out, while the red clump is visible as a thin line above the main sequence, which is the result of dust extinction and reddening. If we use our estimates of

¹⁵ We show in appendix E that an apparent bias can arise if one uses the mean as an estimator when the likelihood is skewed.

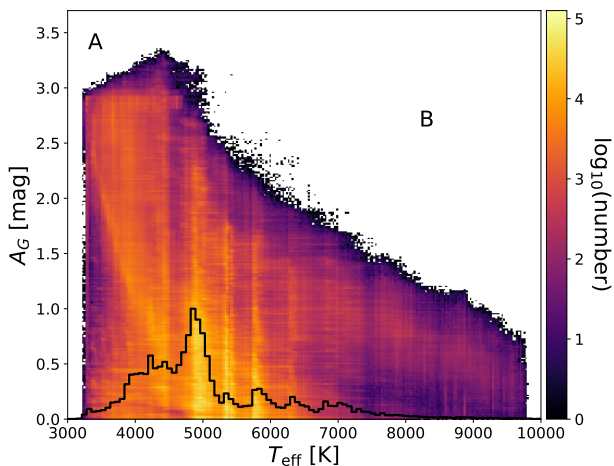


Fig. 18. Variation of Priam A_G with Priam T_{eff} for all stars with clean flags and parallax uncertainty less than 20%. Two unoccupied regions in this plane are marked by “A” and “B”. The black histogram at the bottom shows the total distribution of T_{eff} in our training sample, i.e., the sum over all catalogues shown in Fig. 5. The histogram peaks coincide with the vertical stripes.

A_G and $E(\text{BP-RP})$ in order to correct the observed CMD, then we achieve Fig. 19b. This dust-corrected CMD is much less diffuse. In particular, the red clump is now an actual clump, the main sequence is more compact, and we can identify the giant branch. The horizontal stripes along the main sequence in Fig. 19b are artefacts that originate from the sampling of PARSEC evolutionary tracks which we took directly without further interpolation or smoothing. There are also horizontal streaks above the red giant branch, which are sources with poor parallaxes leading to a clustering in our results. Furthermore, there is a small group of 8587 sources ($\sim 0.01\%$ of all sources that have extinction estimates) just above the main sequence, which either are outliers that we failed to remove (see section 6.5) or which may be genuine binaries. If we additionally require the relative parallax uncertainty to be less than 20% (Bailer-Jones 2015), then the observed CMD becomes Fig. 19c, which is much cleaner than Fig. 19a. The dust-corrected CMD corresponding to this – Fig. 19d – is likewise more distinct. In particular, the horizontal streaks above the giant branch are removed by cutting in relative parallax uncertainty. Nevertheless, Fig. 19 panels b and d also exhibit clear artefacts, some of which are due to bad parallaxes, although most are introduced by our methods and the training data. As all our models are only for single stars, binaries will receive systematically wrong extinction estimates. As most binaries reside above the main sequence, Priam will typically misinterpret them as highly reddened single stars from the upper part of the main sequence. Finally, we note that the logarithmic scale in Fig. 19 overemphasises the low-density regions, intentionally drawing the reader’s attention to the various artefacts. Nevertheless, our results produce a very thin main sequence, as is obvious from Fig. 20 which is exactly identical to Fig. 19b apart from a linear density scale.

The statistical validity of our A_G estimates is further attested to by Fig. 21. Recall that we do not use any sky position during our inference: each star estimate remains independent of any other.¹⁶ This plot shows features quite distinct from just plotting the Gaia colour, as should be obvious from their lack of corre-

lation (shown in Fig. 15). Plotting our extinction estimates on the sky not only highlights the Milky Way disk, but also numerous detailed substructures. Apart from the Small and Large Magellanic Clouds, we also recover a wealth of structure across a wide range of scales, from thin filaments to large cloud complexes. The Perseus, Taurus, and Auriga cloud complexes dominate the anticentral region (far left and right sides of the map, respectively), while the Orion molecular cloud complex ($\ell \sim 210, b \sim -15^\circ$) and the California nebula ($\ell \sim 160, b \sim -8^\circ$) show exquisite substructures, as does Ophiuchus just above the Galactic Center. More will be shown in section 6.7.

5.3. Results for \mathcal{L}

In this and the next subsection we describe the contents and the quality of the catalogue entries for \mathcal{L} and \mathcal{R} . We remind readers that upon validation of FLAME astrophysical parameters, several filters were put in place to remove individual entries, e.g. stars with $\mathcal{R} \leq 0.5 \mathcal{R}_\odot$ have no published radii or luminosities: see Appendix A for details. Only 48% of the entries with T_{eff} also have \mathcal{L} and \mathcal{R} (77 million stars). Unless otherwise specified, we present the results for the published catalogue.

The quality and distribution of the luminosities in the catalogue can be best examined by constructing Hertzsprung–Russell Diagrams (HRD). The HRD using FLAME \mathcal{L} and Priam T_{eff} is shown in the top panels of Figure 22 separated by galactic latitude b ($|b| \leq 45$ and $|b| \geq 45$). For stars at lower galactic latitudes, our neglect of extinction in the luminosity estimation can lead to misinterpretations for individual stars or populations of stars. This can be seen in panel (a) where in particular the red giant branch is extended towards lower T_{eff} , and their luminosities appear lower (see also section 5.1). The vertical stripes at distinct T_{eff} values is a result of the inhomogeneous temperature distribution in the training sample (discussed in section 5.2, see Fig 5). The clean diagonal cut on the lower end is a direct result of our filtering out of sources with $\mathcal{R} < 0.5 \mathcal{R}_\odot$. Replacing T_{eff} by de-reddened color in the abscissa, and including A_G as given in equation 5, we see (in panel c) that the HRD tightens up nicely with a clear structure defining the main expected components. These results clearly highlight the degeneracy between A_G and T_{eff} when only three photometric bands are available, but it also provides a positive validation of the extinction parameters.

For stars at higher galactic latitude we find a very different distribution, where extinction no longer plays a dominant role. Using \mathcal{L} and T_{eff} directly from the catalogue yields a clean HRD with clearly defined components, as shown in panel (b). For reference we show the same sources in panel (d) while including A_G and replacing T_{eff} by de-reddened color.

5.4. Results for \mathcal{R}

The distribution of the radii of our sources for different distances from the Sun are shown in Fig. 23. Here we assume the distance is the inverse of the parallax. Panels (a) and (b) show sources with $\mathcal{R} < 5 \mathcal{R}_\odot$ and $0.5 < \mathcal{R}/\mathcal{R}_\odot < 15$, corresponding roughly to main-sequence and giant stars respectively.

In panel (a) we see that the radius distribution changes with distance and in particular that the mode of the distribution is found at larger radii as we move to larger distances. Such a change in the distributions to within a few kpc should not exist (not least because we are not considering any specific direction).

the Central Limit Theorem applies to any average of our extinction or reddening estimates.

¹⁶ On account of this independence, plus the finite variance (guaranteed by the inability of EXTRATREES to extrapolate beyond the training range),

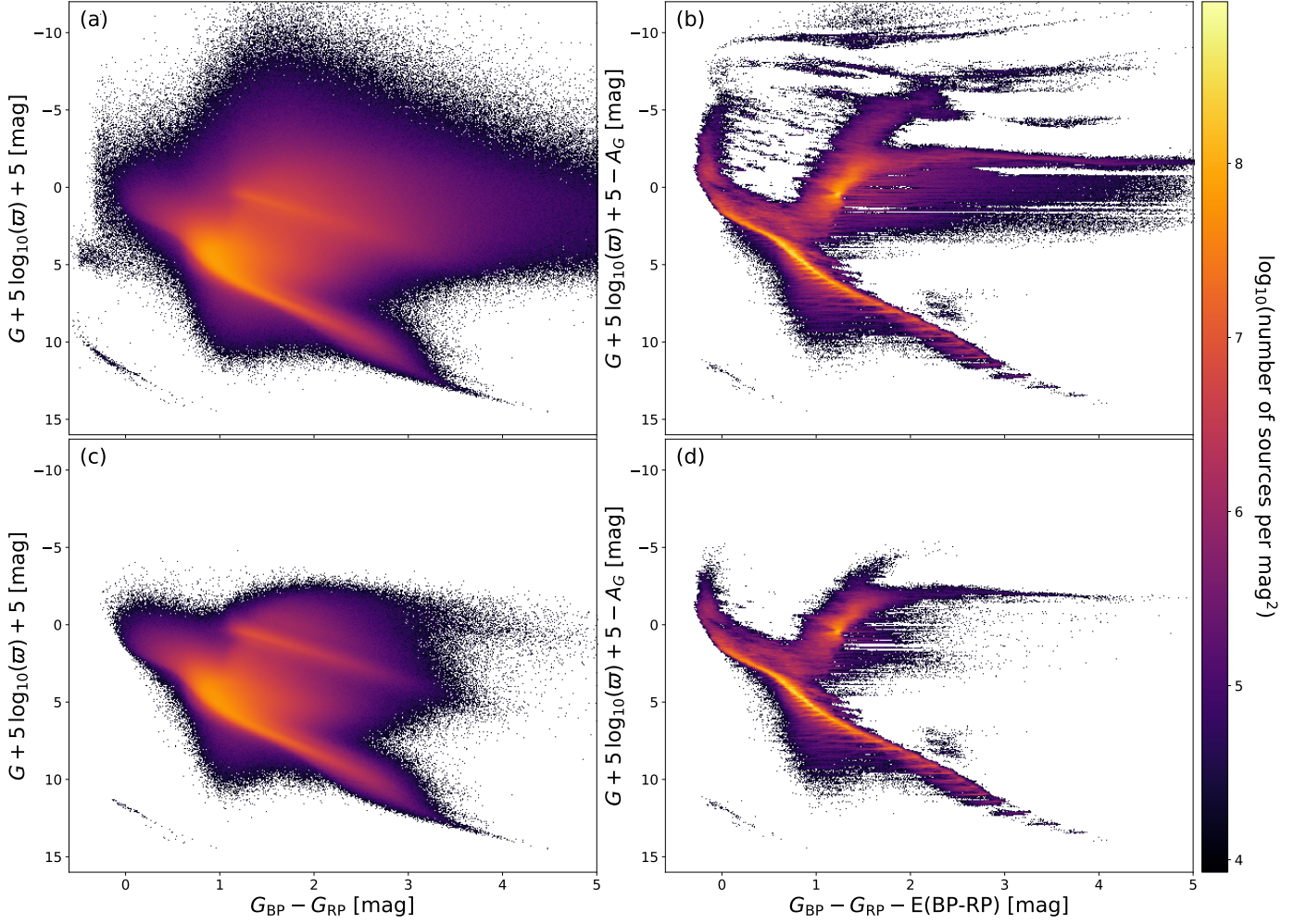


Fig. 19. Observed colour-magnitude diagrams (panels a and c) and dust-corrected colour-magnitude diagrams (panels b and d). Using our estimate of A_G , we obtain M_G from $M_G + A_G (= G + 5 \log_{10} \varpi + 5)$. The upper panels a and b show all sources with $G \leq 17$ and $\varpi > 0$. The lower panels c and d restrict this further to sources with parallax uncertainties lower than 20%.

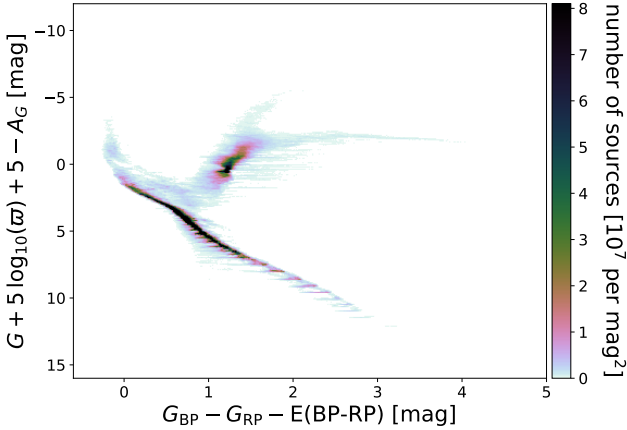


Fig. 20. Same as Fig. 19b but on linear density scale. Some sources, e.g. white dwarfs, have such a low density as to now be invisible on this scale.

This is in fact a selection effect due to the filtering imposed on FLAME parameters (see appendix A). The broader distributions at larger distances are a direct result of this filtering, whereby

stars with sufficiently small diameters and luminosities are removed. For example, due to the magnitude cut at $G = 17$ mag for all astrophysical parameters, no solar-like star will exist in the catalogue for distances larger than approximately 2.5 kpc. Likewise, the FLAME filtering will also remove smaller, fainter stars that have large parallax uncertainties ($\sigma_\varpi/\varpi > 0.2$).

We do not expect to find the same selection effect for more evolved stars, however, and this can be seen in panel (b) where we find distributions that peak between 10 and 11 R_\odot at all distances. This is shown more clearly in panel (c) where we plot the mode of the distributions as a function of distance.

As we have chosen not to include extinction in our calculations of luminosity, we investigate the impact of this assumption on the characterisation of the local population. In general, \mathcal{L} will be underestimated for most stars and as a consequence \mathcal{R} for a fixed T_{eff} will also be underestimated. However, T_{eff} is also partially degenerate with extinction, and a hotter extinguished star could appear cooler (this is shown in section 6.8 for a sample of giant stars). For a fixed \mathcal{L} this would imply a larger \mathcal{R} . For a group of similar stars the impact of the zero extinction assumption should manifest itself as a slow change in the peak radius as the distance increases. We performed a similar analysis as shown in panel (a), but now for less evolved stars in three different temperature ranges: $4800 < T_{\text{eff}} < 5200$, $5600 < T_{\text{eff}} < 6000$, and

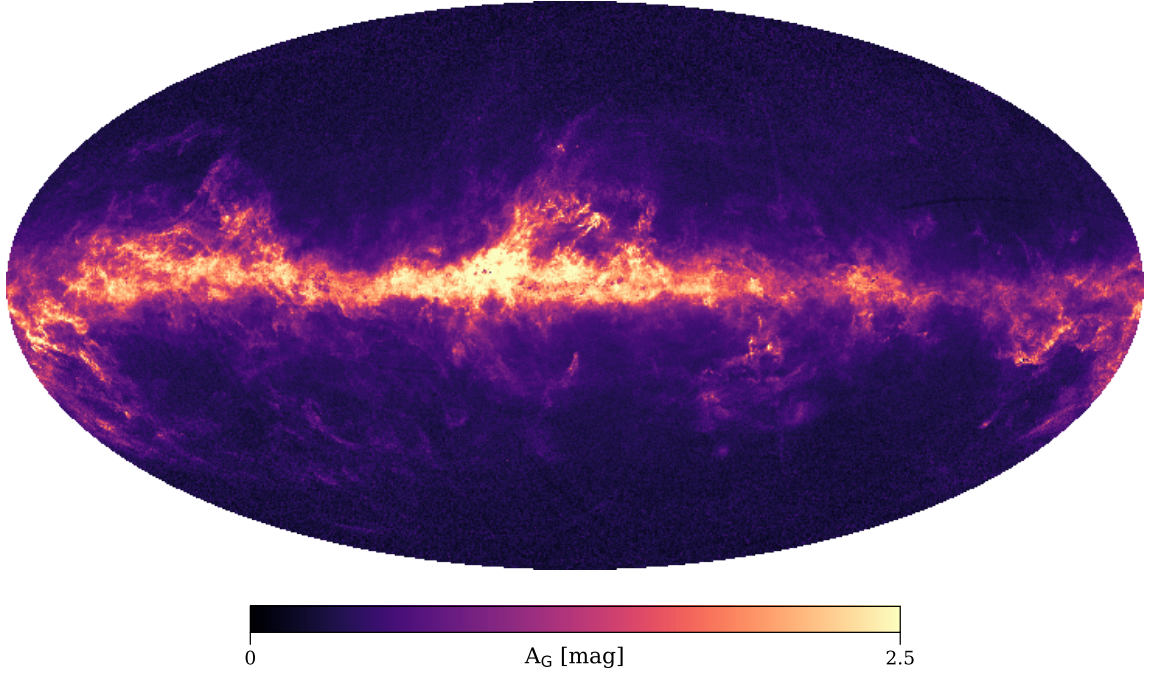


Fig. 21. Distribution of A_G (averaged over all parallaxes) in Galactic coordinates (Mollweide projection). The map is centered on the Galactic Center, with longitudes increasing towards the left.

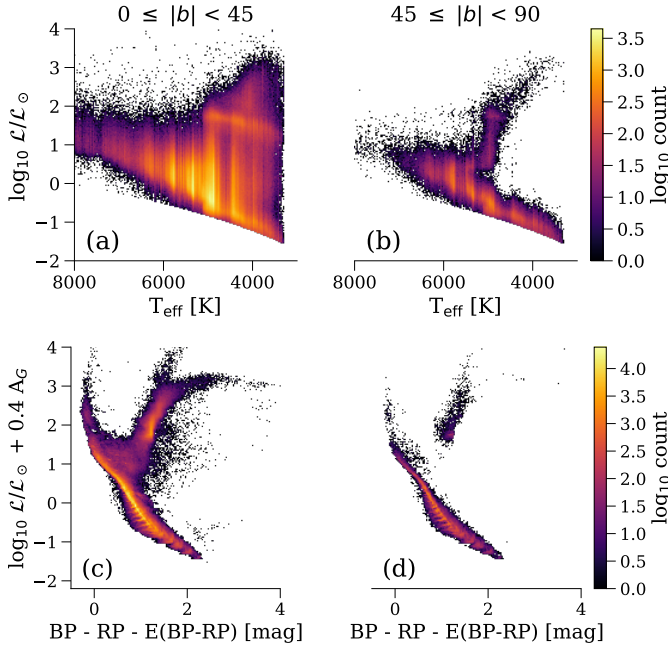


Fig. 22. HRD from Gaia DR2 separated in galactic latitude (left and right). The top panels show \mathcal{L} against T_{eff} and the lower panels show \mathcal{L} against colour, but corrected for extinction.

$6300 < T_{\text{eff}} < 6700$ K. The modes of these distributions as a function of distance are shown as the colour lines in panel (c). For each of the temperature ranges, we can identify at what distance the population is filtered out by the FLAME criteria from a rapid increase in the mode; these are denoted by the '+' symbol. For values below these limits, however, it can also be seen that even with the assumption of zero extinction, the peak increases

very slowly and remains within 5–7% of the value at the closest distances to us, a value consistent with our typical uncertainties. We therefore conclude that the published radii can be safely used (considering their uncertainties) for the less evolved stars, without correcting for extinction.

For the evolved stars (grey dashed line in panel c) we find that the mode of the distribution remains essentially flat as a function of distance. Here it is possible that the impact of setting $A_G = 0.0$ mag on \mathcal{L} and \mathcal{R} is more pronounced than a possible T_{eff} bias from Priam. For these stars, one should consider this fact when using the \mathcal{L} values. However, we expect \mathcal{R} to be affected to a much lesser extent.

6. Validation and comparison with external data

We now validate our results, primarily through comparison with results from non-Gaia sources. Recall that we use the term “error” to refer to the difference between an estimated quantity and its literature estimate, even though one or both could contain errors.

6.1. Temperature errors vs. $\log g$ and $[\text{Fe}/\text{H}]$

Using the test set with literature values for T_{eff} , $\log g$, and $[\text{Fe}/\text{H}]$, Fig. 24 shows how the differences between our temperatures and those in the literature vary with $\log g$ and $[\text{Fe}/\text{H}]$. Other than for the extreme $\log g$ values, the test errors (RMS and bias) show no significant dependence on $\log g$. In particular, dwarfs and giants have the same quality of temperature estimates. For $\log g \geq 4.8$, our T_{eff} estimates are strongly overestimated. This might be because our high $\log g$ stars are generally cool, with spectra dominated by molecular absorption which may complicate the estimation of T_{eff} even when dealing with broad-band integrated photometry. Alternatively it's due to dwarfs being

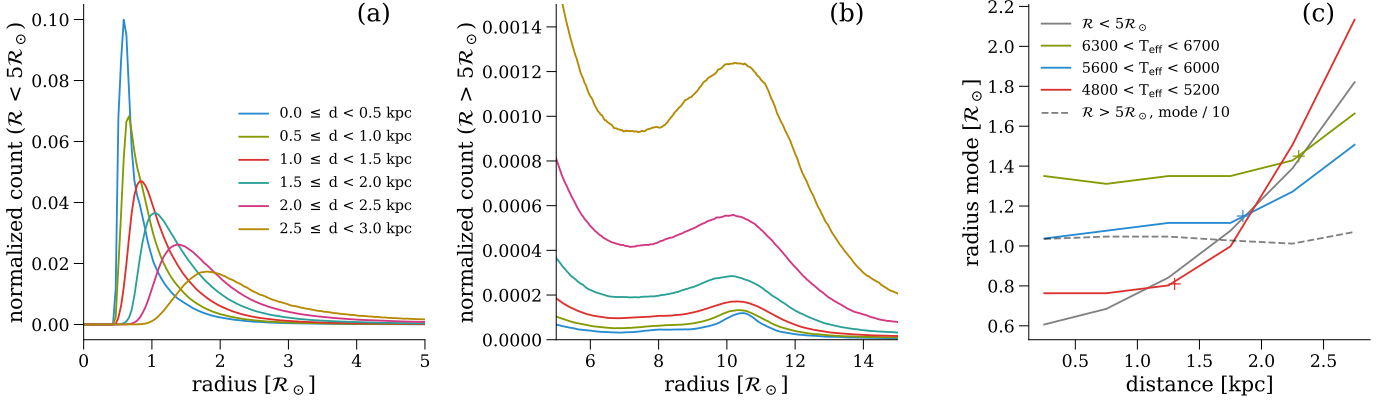


Fig. 23. Distribution of radii for different distance bins (different colours) for stars with (a) $R < 5 R_{\odot}$, and (b) $5 < R/R_{\odot} < 15$. Panel (c) highlights the variation of the mode of the distributions with distance. The crosses indicate to approximately what distance this population of main sequence stars have published radii and luminosities. The solid grey lines and the dashed line show the results corresponding to panels (a) and (b) respectively (the latter scaled by a factor of ten). The coloured continuous lines show the results for $R < 5 R_{\odot}$ but for narrower T_{eff} ranges, in order to isolate the impact of the assumptions on extinction from the FLAME filtering criteria.

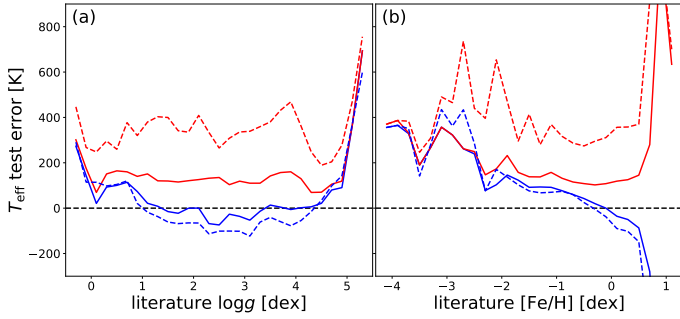


Fig. 24. Dependence of temperature error on literature values of $\log g$ (panel a) and [Fe/H] (panel b) for test data (*not* used for training EXTRATREES) with clean flags. Red lines are root-mean-squared error (dashed) and root-median-squared error (solid) and blue lines are mean error (dashed) and median error (solid).

preferentially nearby and thus generally having a low extinction compared to the mean of the T_{eff} training sample, resulting in an overestimation of T_{eff} (see Fig. 13).

The right panel of Fig. 24 shows that the T_{eff} RMS error increases with decreasing metallicity, with the smallest RMS error (and bias) around solar metallicity. In the range $-2 \lesssim [\text{Fe}/\text{H}] \lesssim 0.5$ our estimates are good, which simply reflects the metallicity distribution in our training sample. Outside this interval, Priam estimates of T_{eff} (and thus the derived FLAME parameters) are more biased. Note that for metal-poor stars, Priam systematically overestimates T_{eff} , which will play a role for halo stars but is probably secondary to the impact of extinction in Fig. 12.

6.2. Stellar types in CMD and HRD

In Fig. 25 we identify stars in our CMDs using classifications from the literature. This demonstrates that different classes of stars appear where we would expect them to.¹⁷ However, Fig. 25b makes it clear that our temperature estimates are unreliable for highly extincted stars, which is the case for these red

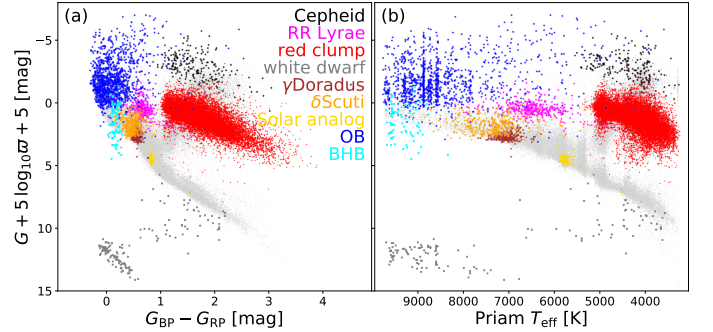


Fig. 25. Colour-magnitude diagram (panel a) and Hertzsprung-Russell diagram (panel b) highlighting stars of known classes (from the literature): Cepheids (Tammann et al. 2003), RR Lyrae (Wils et al. 2006), red clump (Bovy et al. 2014), white dwarfs (Kleinman et al. 2013), γ Doradus and δ Scuti (Sarro et al. 2016), Solar analogues (Tucci Maia et al. 2016), OB (Ramírez-Agudelo et al. 2017; Simón-Díaz et al. 2011, 2017), and BHB (Sirko et al. 2004). We show only stars with clean flags and parallax uncertainties better than 50%. A 20% limit would remove all BHB stars.

clump stars. This is consistent with the fact that we assume low extinction when estimating T_{eff} in Priam. This restriction was necessary given the strong $T_{\text{eff}}-A_G$ degeneracy in the colours used (see section 2.1). Note also that even most of the white dwarfs appear in the right location in Fig. 25b, even though we excluded all white dwarfs from the Priam training sample. There are, however, quite a few white dwarfs that fall between the main, obvious white dwarf sequence and the lower envelope of the main sequence. We see this in both panels of Fig. 25, so it is not an artefact of the Apsis results but rather some problem with the photometry (e.g. blending with a low-mass companion in an unresolved binary system).

6.3. Temperature estimates for very hot and very cool stars

What happens to stars which have true T_{eff} outside the training interval 3000K–10 000K? Intuitively, we would expect that hotter stars are assigned temperatures just below 10 000K, whereas cooler stars are assigned temperatures just above 3000K. This can be seen in Fig. 25b, where most of the OB stars indeed have

¹⁷ Variable stars of course move around in the CMD according to their phase. The photometry is averaged over many observation epochs, so the positions here correspond to some kind of time average which may not be very representative.

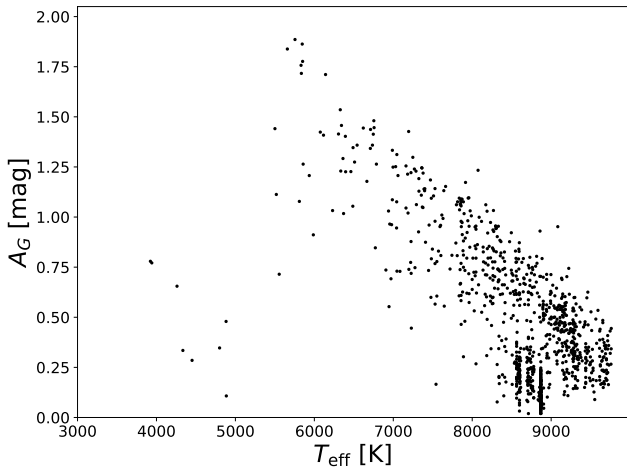


Fig. 26. Priam estimates of T_{eff} and A_G for 1174 stars classified as OB stars by Simón-Díaz et al. (2011, 2017) and Ramírez-Agudelo et al. (2017). Only stars with clean flags are shown.

T_{eff} estimates above 8000K up to the limit of the grid. However, there are also a few cases where OB stars are assigned significantly lower temperatures. Priam infers high extinctions for these (see Fig. 26). Since OB stars often reside in regions with substantial dust, the resulting reddening makes them appear cooler, leading Priam to assign a lower T_{eff} (as explained earlier). The univariate nature of EXTRA TREES is a limitation here, since it prevents a high extinction estimate from being a signal that observed colours may be substantially reddened. (We will use multivariate models in Gaia DR3; see section 8.) Furthermore, the degeneracy between T_{eff} and A_G cannot lead to overestimating OB star extinctions by much, since there are no other models that are intrinsically even bluer than these.

At the lower T_{eff} end, we have eight stars in our test set with literature estimates below 3000K. Of these, seven are assigned T_{eff} below 4000K and the eighth is assigned 4120K. The lower T_{eff} limit is obviously better behaved than the upper temperature limit, where extinction is leading to additional confusion.

The inability of EXTRA TREES to extrapolate from its training label range of 3000K – 10 000K does not only apply to the median but also to the 16th and 84th percentiles serving as uncertainty estimates. Consequently, the uncertainties cannot appropriately reflect the underestimation of T_{eff} for OB stars, for example.

6.4. Solar analogues and Gaia benchmark stars

As mentioned in section 5.1, the error in our temperature estimates depends strongly on the temperature distribution of the sample under consideration. Here we look at a sample of 88 solar analogues from Tucci Maia et al. (2016), of which 70 were in our processing and have clean flags. As shown in Fig. 27, most of our T_{eff} estimates are close to the solar value of 5772K (see Table 3). Excluding the eight solar analogues that were part of the training sample for EXTRA TREES, the RMS test error for the remaining 62 stars is just 73K (1.3%), which is much smaller than the mean RMS error of 324 K reported in section 5.1. The likely explanation for this excellent performance is that the solar temperature is very close to the mean temperature in our training sample (see Fig. 5), which is where machine learning algorithms usually perform best.

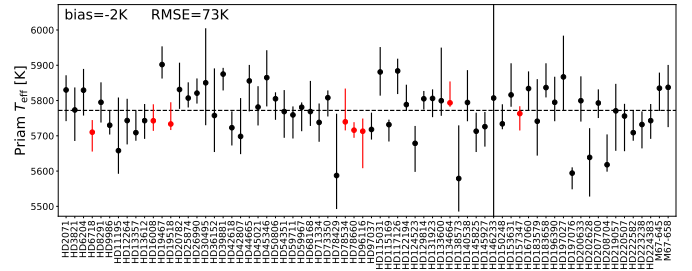


Fig. 27. Priam estimates of T_{eff} for 70 solar analogues with clean flags from Tucci Maia et al. (2016). The horizontal dashed line indicates the accepted solar value of 5772K (see Table 3). Red points were part of the EXTRA TREES training sample so are excluded from the bias and RMS error computations shown in the top left corner.

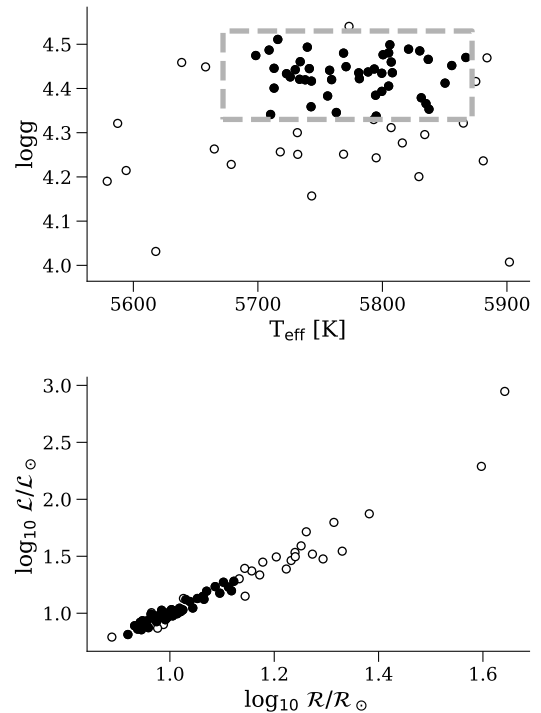


Fig. 28. T_{eff} , $\log g$, \mathcal{R} , and \mathcal{L} (computed from our results) for the 70 solar analogues. The solid points have T_{eff} within 100 K of the Sun and $\log g$ within 0.1 dex of the Sun (highlighted by the box in the upper panel).

Regarding our uncertainty estimates, we find that the solar temperature is below our lower uncertainty level in 23% of cases, and above the upper uncertainty level for 29% of cases. This agrees with our findings from section 5.1.

All of the 70 solar analogues found in our catalogue have valid parallaxes and so \mathcal{L} and \mathcal{R} were derived. We can estimate their surface gravities ($\log g$) using \mathcal{R} and assuming solar mass. These are shown in Fig. 28. We refine our selection of solar analogues by requiring T_{eff} to be within 100 K of the Sun and $\log g$ within 0.1 dex. This leaves 46 better analogues, shown as filled circles in Fig. 28. We can see this more clearly in the lower panel of Fig. 28. The importance of adding the parallax, magnitude, and \mathcal{R} to distinguish between what we consider solar analogues is evident. Using this set of 46 better solar analogues we derive a mean $M_G = 4.65 \pm 0.13$ from their G and ϖ values. By assuming their $M_{\text{bol}} = M_{\text{bol}\odot}$, we obtain a mean value of $BC_G = +0.09$ mag for these solar analogues, which is in good agreement with our

adopted value for the Sun of $BC_{\odot} = +0.06 \pm 0.10$ mag from section 4.1 (derived in appendix D).

16 of the 34 Gaia benchmark stars (Heiter et al. 2015) are in Gaia DR2 (the missing 18 are too bright for the current processing). All have T_{eff} estimates from Priam: the RMS difference with respect to Heiter et al. (2015) is 230 K, which includes a mean difference of -24 K. However, only 6 of the 16 benchmark stars have parallaxes and thus FLAME results, and the RMS difference of \mathcal{L} to Heiter et al. (2015) is 13.1%, which includes a mean difference of -3.7% .

6.5. Ensemble extinction at high Galactic latitudes

We can validate our extinction estimates using stars at high Galactic latitudes, $|b| > 50^\circ$, where we expect the true extinction to be close to zero, especially for nearer stars (e.g. Schlegel et al. 1998; Schlafly et al. 2015). However, as our method cannot produce negative extinctions, and given the presence of noise, it is obvious that the average extinction for any ensemble of stars must be larger than zero. Here we study this effect and compare it to our expectations from simulations. We use extinction and reddening estimates for the full sample which is not available to the reader due to the filtering of outliers described in this section. We also derive global uncertainty estimates for A_G and $E(\text{BP} - \text{RP})$.

Fig. 29a shows the distribution of A_G for high Galactic latitude stars (black histogram). The distribution is clearly peaked at zero extinction and roughly follows an exponential distribution (see below). In particular, 74% of these high Galactic latitude stars have extinctions below 0.5 mag (in the Gaia DR2 sample 82% of them have $A_G < 0.5$ mag due to the removal of outliers). Nonetheless, there is a prominent tail extending to extinction values as large as $A_G \simeq 3$ mag. We also show simulation results (orange histogram) where we applied Priam to synthetic sources from PARSEC which had zero extinction. This produces a similarly heavy tail (note that the distribution is hardly changed if we add typical Gaia noise to the simulated photometry).

The origin of this heavy tail is revealed by Fig. 29b, where two pronounced groups of stars with large extinctions (“outliers”) emerge, one around $G_{\text{BP}} - G_{\text{RP}} \simeq 1$ mag and the other at $G_{\text{BP}} - G_{\text{RP}} \simeq 2.3$ mag. These outliers, while relatively few in number (note the colour scale), are assigned unreasonably large extinctions. We see these in Fig. 29c as the two yellow patches on the upper envelope of the main sequence, one around $G_{\text{BP}} - G_{\text{RP}} \simeq 1$ mag and the other around $G_{\text{BP}} - G_{\text{RP}} \simeq 2.3$ mag. Both cases are a consequence of the strong degeneracy of extinction with temperature: The observed red colour can be incorrectly interpreted as an intrinsically bluer and brighter star being made redder and fainter through extinction. We see high extinction in those regions of the CMD where such hotter but extincted stars in the Priam training set can appear. The same behaviour occurs in the simulation shown for comparison in Fig. 29a, where we see a long tail to high extinctions. We conclude that these outliers are the result of an unfortunate alignment of the extinction vector with the astrophysically allowed states in the CMD as defined by the PARSEC training sample. This is a fundamental limitation imposed by having only three broad optical bands (G , G_{BP} , G_{RP}). The BP/RP spectra should enable us to largely overcome this problem in Gaia DR3 (see section 8).

These outliers were removed from the Gaia DR2 catalogue according to the following criteria. The degeneracies are caused by model stars with different extinctions and reddenings (and different stellar parameters) having the same apparent magni-

tudes. In such a case, the EXTRATREES ensemble provides a wide range of estimates over all these degenerate states, since it cannot distinguish among them. As our uncertainty estimates are a measure of this spread, such outliers will have large uncertainty intervals. Thus, Gaia DR2 only retains estimates of A_G and $E(\text{BP} - \text{RP})$ for sources which satisfy the following conditions

$$\frac{A_G^{\text{upper}} - A_G}{A_G - A_G^{\text{lower}}} > 0.4, \quad (8)$$

$$A_G - A_G^{\text{lower}} < 0.5, \quad (9)$$

$$\frac{E(\text{BP} - \text{RP})^{\text{upper}} - E(\text{BP} - \text{RP})}{E(\text{BP} - \text{RP}) - E(\text{BP} - \text{RP})^{\text{lower}}} > 0.4 \quad \text{and} \quad (10)$$

$$E(\text{BP} - \text{RP}) - E(\text{BP} - \text{RP})^{\text{lower}} < 0.3. \quad (11)$$

A_G^{lower} and A_G^{upper} refer to the 16th and 84th percentiles respectively and likewise for $E(\text{BP} - \text{RP})^{\text{lower}}$ and $E(\text{BP} - \text{RP})^{\text{upper}}$. The first two filters are justified by Fig. 30. A similar figure justifying the latter two can be found in the online documentation. Of the 161 million sources with extinctions from Apsis, 88 million pass these criteria and so have extinctions in Gaia DR2. While this removes most of the outliers, it is of course not perfect. Unfortunately, the filters also remove many stars on the main sequence turn-off and the lower giant branch. The complete CMD before applying these filters is shown in Fig. 31, which should be compared directly to Fig. 19d to see the impact of the filtering.

We now return to the sample of high Galactic latitude stars ($|b| > 50^\circ$) with this filtering applied. This results in the A_G distribution shown in Fig. 32. It agrees very well with an exponential distribution of mean 0.30 mag and its standard deviation from zero extinction, $\sqrt{\langle A_G^2 \rangle}$, is 0.46 mag. The fact that Fig. 32 is largely consistent with an exponential distribution is important, because this suggests these high Galactic extinction values are consistent with truly zero with random noise according to information theory: if A_G values are pure noise then its distribution follows its maximum entropy distribution, and with a positivity constraint this distribution is an exponential (e.g. Dowson & Wragg 2006). If the true extinction of high Galactic latitude stars is zero, then our method will infer a positive value which is just noise; the distribution over these extinctions must therefore be the maximum entropy distribution for a non-negative real-valued quantity, which is an exponential. Since Fig. 32 is very consistent with an exponential distribution, this is evidence that A_G is pure noise for high Galactic latitude stars.¹⁸

The reddening is also largely consistent with an exponential, of mean 0.15 mag and a standard deviation about zero, $\sqrt{\langle E(\text{BP} - \text{RP})^2 \rangle}$, of 0.23 mag.

From these results we obtain “global” uncertainty estimates for A_G and $E(\text{BP} - \text{RP})$ of 0.46 mag and 0.23 mag, respectively. These are slightly larger than our comparisons to literature values of A_V and $E(B - V)$ from Table 6, but we take these as estimates of our overall uncertainties.

6.6. Red clump stars

As discussed earlier (section 5.2), our estimates of A_G and $E(\text{BP} - \text{RP})$ show a large RMS error on a test sample, so are

¹⁸ The agreement with an exponential is not perfect, as is obvious from Fig. 32b. Possible explanations are an imperfect removal of outliers and genuine extinction features at high Galactic latitudes such as young clusters.

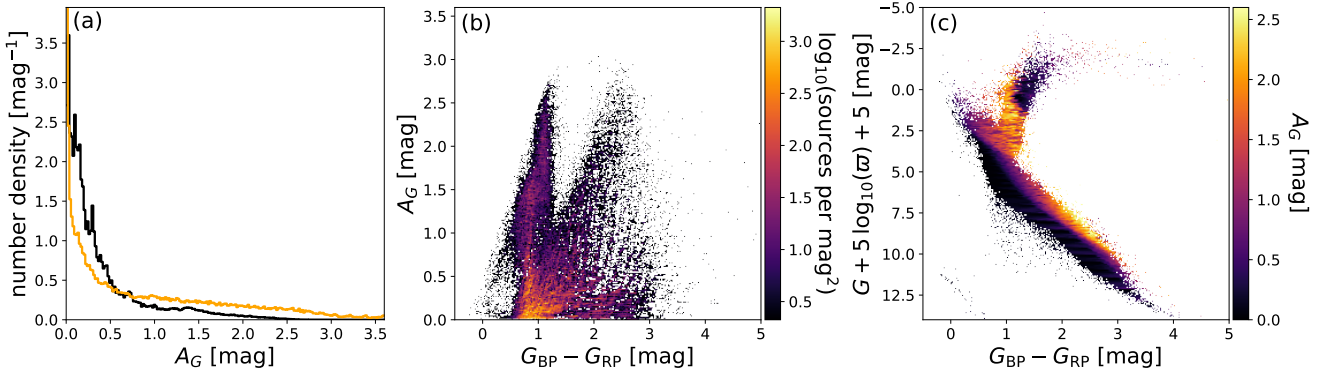


Fig. 29. Extinction estimates of high Galactic latitude stars with $|b| > 50^\circ$ and parallax uncertainty better than 20% before applying the filters of Eqs. (8)–(11). Panel a: Distribution of A_G values (black), and distribution of simulation results with PARSEC photometry for $A_0 = 0$ and $[\text{Fe}/\text{H}] = 0$ (orange). Panel b: Density of sources in colour–extinction space showing two sets of outliers with unexpectedly large A_G estimates at $G_{\text{BP}} - G_{\text{RP}} \approx 1$ mag and ≈ 2.3 mag. Panel c: Colour–magnitude diagram highlighting the location of these two sets of outliers.

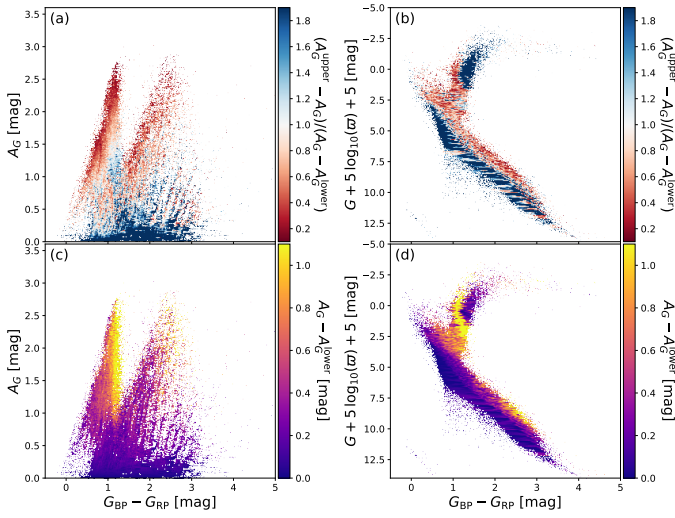


Fig. 30. Identification of the most degenerate extinction estimates for high Galactic latitude stars with $|b| > 50^\circ$ before applying the filters of Eqs. (8)–(11). Panels a and b show the identification via the asymmetry of confidence intervals. Panels c and d show the identification via the lower confidence interval. A corresponding plot for $E(\text{BP} - \text{RP})$ is provided in the online documentation.

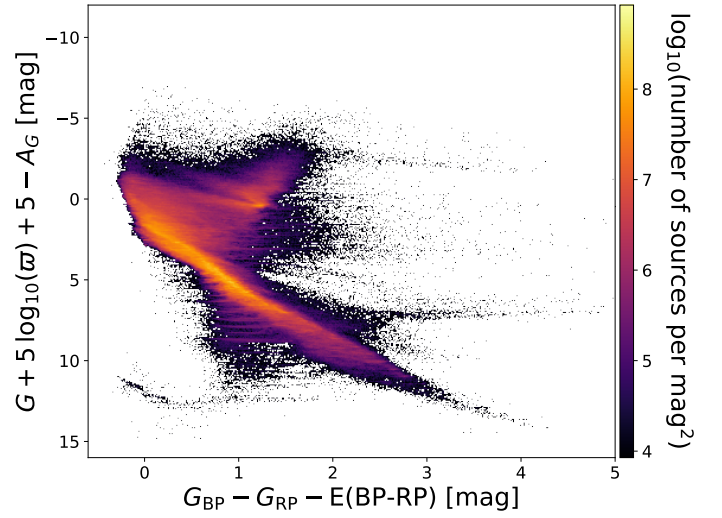


Fig. 31. Dust-corrected colour–magnitude diagram from complete results (not available in Gaia DR2). Same as Fig. 19d but before applying the filters from Eqs. (8)–(11).

generally only useful when combined in an ensemble. We examine here our extinction estimates for red clump stars from Bovy et al. (2014) in order to derive a global uncertainty estimate for A_G and $E(\text{BP} - \text{RP})$. We found 18 957 of their red clump stars in the Gaia DR2 sample with $G < 17$, whereby 15 876 still had extinction and reddening estimates after applying the filters from equations (8)–(11). Using PARSEC models (Bressan et al. 2012) with $A_0 = 0$, $Z = 0.0152$, and evolutionary stage “4”, we estimate that red clump stars reside in a box with a central absolute magnitude of $M_G = 0.51 \pm 0.25$ mag (which agrees with Ruiz-Dern et al. 2017) and a central colour of $G_{\text{BP}} - G_{\text{RP}} = 1.23 \pm 0.05$ mag. In Fig. 33 panels a and b we plot the observable $G + 5 \log_{10} \varpi + 5$ computed from the Gaia data (which is equal to $M_G + A_G$), against our estimate of A_G . For 12 127 red clump stars with parallax uncertainties below 20%, we indeed find a relation that is consistent with the absolute magnitude inferred from the PARSEC models. Likewise, if we plot the observed $G_{\text{BP}} - G_{\text{RP}}$ colour against our estimated $E(\text{BP} - \text{RP})$,

we also find results that are consistent with the intrinsic colour inferred from PARSEC (Fig. 33 panels c and d). Even though many red clump stars have APOGEE metallicity and abundance estimates (Alam et al. 2015) that differ from solar metallicity, thus violating our model assumptions from section 3.3, there are no obvious biases. Using the method described in Appendix C, we find that our estimates of A_G and $E(\text{BP} - \text{RP})$ differ from the observables $M_G + A_G$ and $G_{\text{BP}} - G_{\text{RP}}$ by about 0.21 mag and 0.09 mag, respectively. These uncertainty estimates are substantially smaller than the global uncertainty estimates of 0.46 mag for A_G and 0.23 mag for $E(\text{BP} - \text{RP})$ that we obtained from high Galactic latitude stars in section 6.5. This suggests that our extinction and reddening estimates work better for red clump stars. Furthermore, we find that our estimates of A_G and $E(\text{BP} - \text{RP})$ are unbiased, since for panels b and d in Fig. 33, the resulting intercept estimates (obtained from appendix C) of 0.27 mag for $G + 5 \log_{10} \varpi + 5$ and 1.22 mag for $G_{\text{BP}} - G_{\text{RP}}$ agree very well with the absolute magnitude and intrinsic colour inferred from PARSEC models. Note that the red clump selection by Bovy et al. (2014) may also contain a few RGB stars, contaminating our analysis. Furthermore, there is an intrinsic spread in the ab-

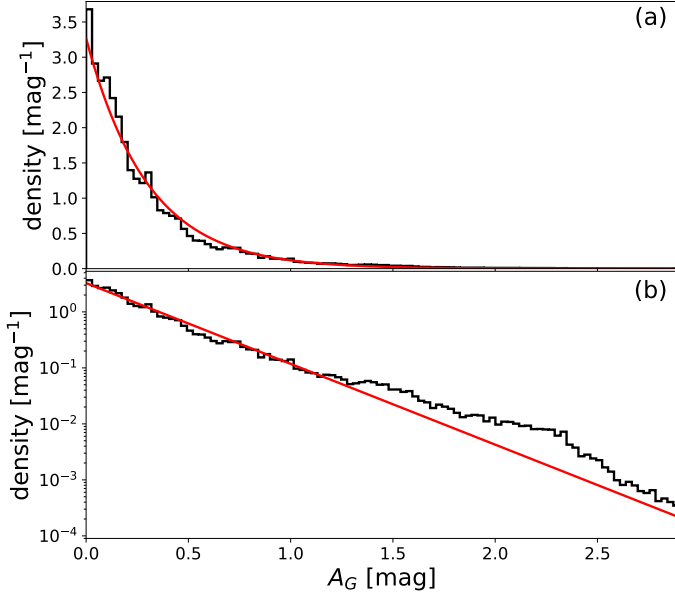


Fig. 32. Distribution of A_G for high Galactic latitude stars with $|b| > 50^\circ$ after applying the filters from Eqs. (8)–(11) (black histogram). The red line shows an exponential whose mean value is set to the mean extinction of this sample, which is 0.30 mag. Panels a and b show both distributions in linear and logarithmic scale, respectively.

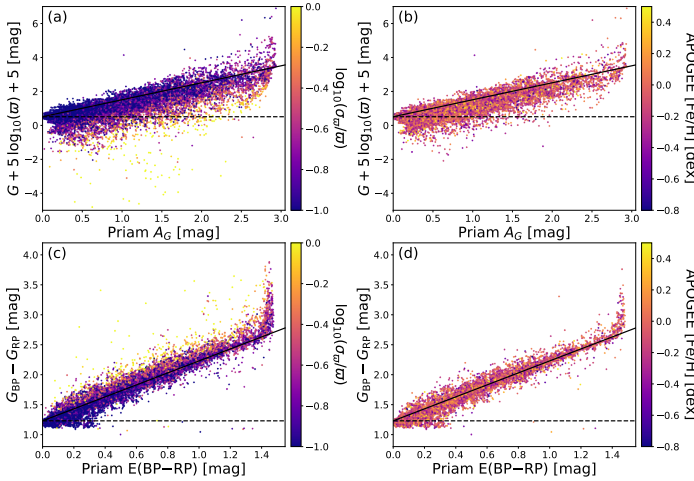


Fig. 33. Priam estimates of A_G and $E(\text{BP} - \text{RP})$ for red clump stars from Bovy et al. (2014). Note that $G + 5 \log_{10} \pi + 5 (= M_G + A_G)$ is an observable. The horizontal dashed lines show $M_G = 0.51$ mag for $A_G = 0$ and $G_{\text{BP}} - G_{\text{RP}} = 1.23$ mag for $E(\text{BP} - \text{RP}) = 0$, which are the approximate absolute magnitude and intrinsic colour of the red clump. The diagonal line is not a fit but the locus of constant absolute magnitude where we expect extinguished red clump stars to lie. Panels a and c: All red clump stars, colour-coded by relative parallax uncertainty. Panels b and d: Red clump stars with parallaxes uncertainties better than 20%, colour-coded by metallicity estimates from APOGEE (Alam et al. 2015).

solute magnitude and colour of the red clump. We neglect this, so our uncertainty estimates of A_G and $E(\text{BP} - \text{RP})$ for red clump stars are conservatively large. Finally, note that the sharp upturn around $E(\text{BP} - \text{RP}) \approx 1.5$ in Fig. 33d suggests that some of the red clump stars may be subject to such strong extinction that they are not covered by our model grid (which extends to $A_0 = 4$ mag).

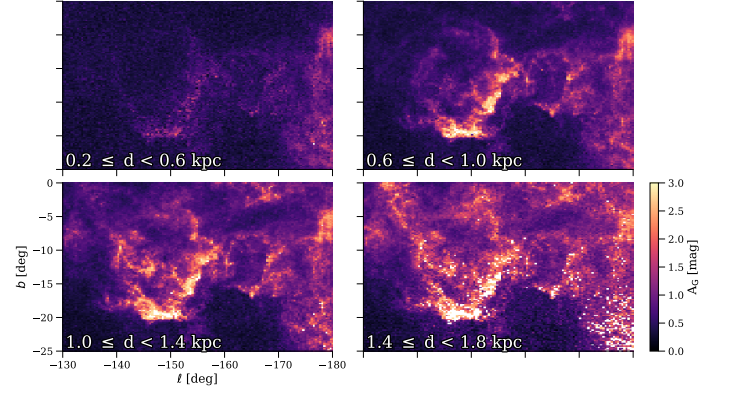


Fig. 34. Extinction estimates toward Orion for different distance slices, from sources with parallax precisions better than 20%. White points lack extinction estimates. Compare to Fig. 2 in Schlafly et al. (2015).

6.7. Dust towards Galactic clusters and nebulae

Schlafly et al. (2015) have investigated the three-dimensional structure of the line-of-sight extinction A_V for the Orion nebula. We show in Fig. 34 our A_G estimates in the same way as Fig. 2 of Schlafly et al. (2015). Each cell shows the mean extinction over the distance range given. As noted in appendix E, this is likely to be an overestimate when the true extinction is low. The agreement is nonetheless striking, although we are missing the fainter stars due to the $G \leq 17$ limit in our processing.

To further assess the quality of our estimates of dust attenuation, we studied the colour–absolute magnitude diagrams of some Galactic star clusters. Fig. 35 shows three examples, with members taken from Gaia Collaboration et al. 2018a who selected them based on their spatial positions and proper motions. The plot shows good agreement with isochrone models of matching age, metallicity, and extinction from Castellani et al. (2002). The colour scale shows the extinction estimates from Priam. The sequences above and parallel to the main sequence in both clusters are presumably binaries. These tend to have larger (overestimated) extinctions. As binaries have slightly redder colours than single stars of the same brightness due to the generally lower mass companion, yet have the same parallax, Priam – assuming all stars to be single – interprets their redder colours to be a result of extinction. (Binary stars will receive explicit treatment in future Gaia data releases; see section 8.)

We show in appendix E that, because our extinction estimates are non-negative, the mean of a sample of stars is often a biased estimator of the true (assumed common) extinction. We can instead use a likelihood function for each star which respects this non-negativity, namely a truncated Gaussian. When we do this, the maximum of the likelihood for the set of cluster members is $A_G = 0.21^{+0.05}_{-0.08}$ mag for the Hyades, $A_G = 0.11^{+0.06}_{-0.07}$ mag for the Pleiades, and $A_G = 0.00^{+0.08}_{-0.00}$ mag for Praesepe (the uncertainties refer to the 16th and 84th percentiles on the likelihood). These cluster extinction estimates are in very good agreement with the values from Castellani et al. (2002) and Taylor (2006), listed in Fig. 35, for the Pleiades and Praesepe clusters. Our estimate for the Hyades, in contrast, is much larger than the literature value. As discussed in appendix E, we suspect this is just a combination of bad luck and a relatively small number of members for precisely locating the maximum of the likelihood. Finally, we note that even within our clean sample, our results in

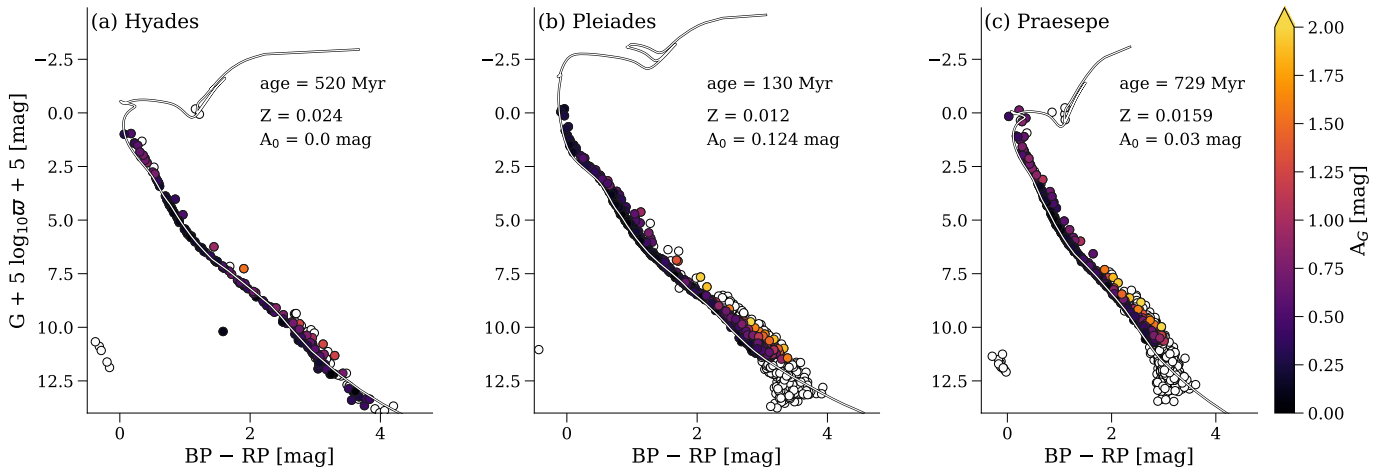


Fig. 35. Colour magnitude diagrams for the Hyades, Pleiades, and Praesepe star clusters. In each panel we indicate cluster members (defined by Gaia Collaboration et al. 2018a) using filled circles coloured according to their extinction estimates (white symbols are members without published extinction estimates in Gaia DR2). The solid lines indicate the PARSEC isochrones with parameter values, marked in the figure, taken from the estimates for the clusters from Castellani et al. (2002) for the Hyades and Pleiades and from Taylor (2006) for Praesepe.

clusters may suffer from photometric errors induced by crowding.

6.8. Validation of radii and luminosities with seismology, interferometry, and surveys of nearby stars

To validate the results for FLAME, we compare the derived radii and luminosities with those from a selection of external catalogues. These are shown in Fig. 36, whereby the targets are mostly bright ($G < 12$) and nearby (< 1500 pc). The top panels compare the radii from a compilation of asteroseismic and interferometric references as a function of literature radii (panel a) and T_{eff} (panel b). For the less evolved stars ($R < 3.0 R_{\odot}$) the FLAME radii are slightly overestimated, but the differences are consistent with zero considering the radius uncertainties for this range (Fig. 9), due to the differences in the adopted temperature scales. The green triangles represent radii from automatic asteroseismic analysis using scaling relations, where typical uncertainties in the radius can be 5% and the actual values of the radii are rather sensitive to the input T_{eff} (see Chaplin et al. 2014). For this sample we also find a systematic trend in the radii which increases with decreasing T_{eff} (panel b). This suggests that the differences in the radii arises from the different temperature scales used. The other stars in this less evolved sample range have been studied in much finer detail using interferometry or detailed asteroseismic analysis (black and blue stars). In these cases, the literature radii are much less sensitive to the adopted T_{eff} . For these better-studied stars, we do find much better agreement with the FLAME radii ($< 5\%$), with no significant differences as a function of T_{eff} .

The largest sample in this figure is that from Vrad et al. (2016), who studied red giants using asteroseismic scaling relations in an automatic manner. For the giants, typical uncertainties in the asteroseismic radii are of the order 7–10% and the radii are sensitive to the adopted T_{eff} . As explained earlier, we ignore interstellar extinction, and thus the luminosities will be systematically underestimated. This is particularly problematic for giants which are more distant, as extinction could be non-negligible. However, for a fixed T_{eff} a smaller luminosity implies a smaller radius. In most cases we see that the radii are underestimated

(negative differences). However, in the range $8 < R/R_{\odot} < 12$ there is a large scatter around zero (there are many overestimated radii too). This zero offset is a direct result of the cancellation effects of the adopted temperature scales and of ignoring extinction. For this sample of stars, we find systematically lower T_{eff} with Priam, where the typical differences are between -5% and -1% . As a consequence, for fixed luminosity, the radius will be overestimated by FLAME. As with the main sequence stars, the interferometric sample (blue stars) and the giants in NGC 6819 (black triangles), which were studied in much finer detail, agree with the FLAME radii to within 10%, and show no trend in their differences as a function of radius or T_{eff} .

In the lower panels of Fig. 36 we compare our estimates of \mathcal{L} and R with those derived from external analyses based on photometric measurements. The left panel (c) compares our luminosities with those derived from the bolometric flux estimates from Casagrande et al. (2011). We also compared our radii using their bolometric flux and temperature measurements (not shown). We obtain a negligible mean difference in the luminosities and radii which can be rectified by changing the $BC_{G_{\odot}}$ by a few mmag (see appendix D). We find a dispersion below 5%, suggesting no unknown systematic effects in our results. In the lower right panel (d) we compare FLAME radii with those derived from predicted angular diameters from Bourges et al. (2017). Again we find a mean offset in the differences close to zero and a dispersion about this mean of less than 10%. In both figures, the blue filled circles represent a subset of these data which fulfil the criteria Priam $\sigma(T_{\text{eff}})/T_{\text{eff}} < 3\%$, $7 < G < 10$, Gaia $\sigma_{\pi}/\pi < 5\%$, and $1/\pi < 300\text{pc}$. These were used to test the $BC_{G_{\odot}}$ discussed in appendix D. The open black circles are stars retrieved in our validation data which don't fulfil these criteria.

7. Using the data

In this work we have, independently for each source, inferred five parameters from three partially degenerate flux measurements and (for all but T_{eff}) a parallax. This has necessarily demanded a number of extreme simplifications and assumptions. The data should therefore be used with great care. We recommend always using the flags, defined in appendix B, to filter out

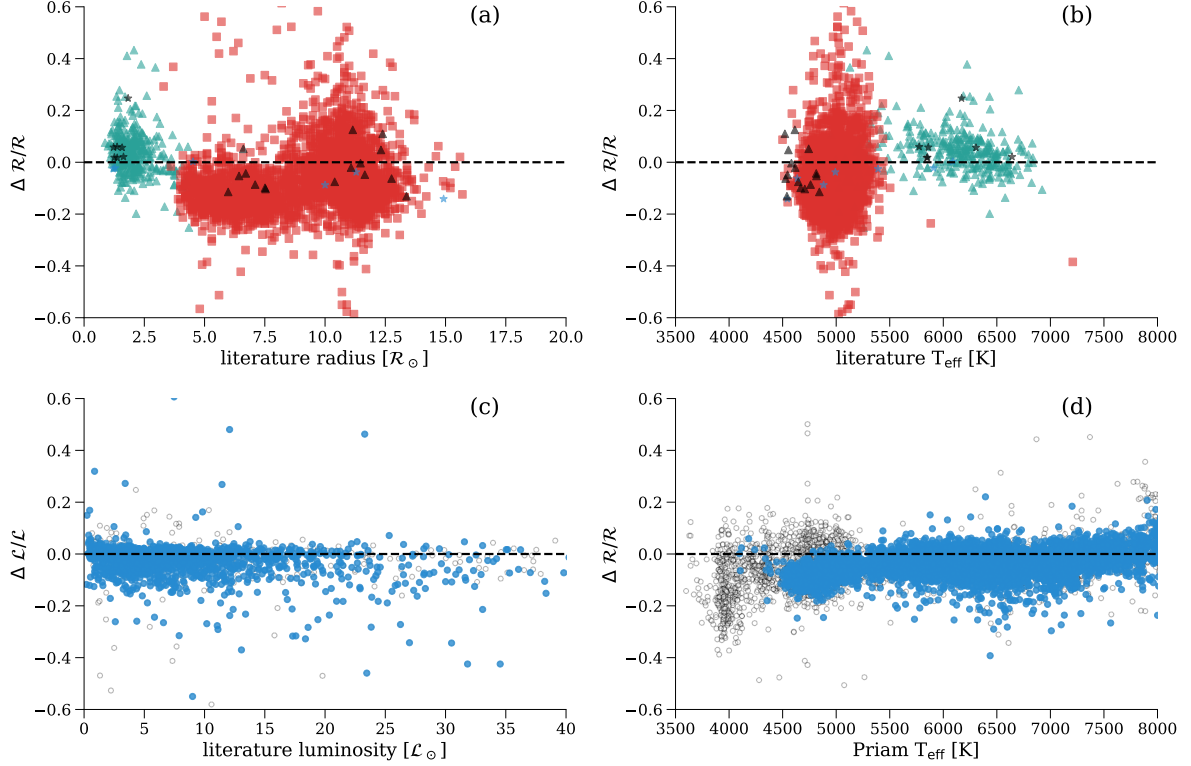


Fig. 36. Comparison of \mathcal{R} and \mathcal{L} with external data. Δ is defined as $(\text{FLAME} - \text{literature})/\text{literature}$. (Top) Comparison of radii as a function of (a) radius and (b) T_{eff} , for asteroseismic and interferometric targets. The symbols indicate different literature sources: red squares are Vrard et al. (2016); green triangles are Chaplin et al. (2014); blue stars are Boyajian et al. (2013) and Ligi et al. (2016); black stars are Creevey et al. (2017); black triangles are members of NGC 6819 from Basu et al. (2011). (Bottom) Comparison of (c) FLAME luminosities with those from Casagrande et al. (2011) and (d) FLAME radii with those from Bourges et al. (2017). The blue circles are the subsample of stars used to estimate BC_{G0} (see appendix D). The open black circles are other stars not fulfilling the stricter criteria for this estimate.

poorer data. In particular, for astrophysical analyses, we recommend only using parameters for stars in the clean T_{eff} sample (defined in that appendix). When using extinctions, luminosity, and radii users may also want to only select stars with small fractional parallax uncertainties (Fig. 19 gives an example of the impact of this filtering on the CMD.)

7.1. Limitations and caveats

The following caveats should be kept in mind.

1. All sources are treated as single stars. We do not perform source classification and our processing does not make use of external classifications. We do not filter out results for sources we know from other data to be galaxies, unresolved binaries, etc.
2. The training sample for T_{eff} of EXTRA TREES contains stars with a certain range of (low) extinctions (see section 3.2). The T_{eff} estimates will be systematically too low when the true extinction is significantly below this range (e.g. in the halo). Likewise, T_{eff} estimates will be systematically too high when the extinction is above this range. One manifestation of this is a systematic trend in temperature errors (from comparison to literature estimates) with Galactic latitude (see Fig. 12). Hot stars with high extinction get T_{eff} estimates that are systematically too low (see Fig. 18). See also Fig. 11e.
3. For T_{eff} estimation, EXTRA TREES was only trained on the range 3000K–10 000K. Stars which are truly hotter or cooler

will therefore be systematically under- or overestimated. However, for A_G and $E(\text{BP} - \text{RP})$ estimation, EXTRA TREES was trained on PARSEC models with $0 \leq A_0 \leq 4$ mag and $2500 \text{ K} \leq T_{\text{eff}} \leq 20\,000 \text{ K}$. While we cannot get T_{eff} estimates from those models, we still get reliable extinction and reddening estimates for intrinsically blue sources such as OB stars.

4. Due to the distribution of parameters in the training sample, the resulting temperature distribution exhibits artificial stripes (see Fig. 18). This also affects the Hertzsprung-Russell diagram (see Fig. 22 and Fig. 25b).
5. The (empirical) T_{eff} training sample lacks low metallicity stars, so systematic errors in T_{eff} can be expected for truly low metallicity stars. The same can be said for the extinction estimates, as our (synthetic) training sample is solar metallicity.
6. As we use three broad optical bands, our estimates of A_G and $E(\text{BP} - \text{RP})$ are highly degenerate with our T_{eff} estimates. This leads to unreliable extinction and reddening estimates in parts of the CMD (see section 6.5).
7. Our extinction estimates are strictly non-negative, with uncertainties of similar size to the estimate itself. Hence neither A_G nor $E(\text{BP} - \text{RP})$ can be considered as a Gaussian random variable, not even approximately. The likelihood (probability density) is intrinsically skewed, which is why we report 16th and 84th percentiles to reflect the uncertainty. As explained in appendix E, a truncated Gaussian is a more appropriate likelihood model for the extinctions. The non-negativity can feign a systematic overestimation of extinction in regions where very low extinction is expected, such as at high Galac-

tic latitudes (section 6.5) or for some stellar clusters (section 6.7). As we show in appendix E, the mean extinction in such regions is a poor estimator of the true extinction.

8. The estimates of A_G and $E(\text{BP} - \text{RP})$ generally have such large uncertainties that their usefulness for individual stars is limited. These estimates should generally only be used statistically, by applying them to ensembles of stars. The central limit theorem applies despite the non-negativity, ensuring that the variance in the mean of a sample will drop as $1/N$, even though the mean may be a biased estimator. The Galactic extinction map (Fig. 21) and the Orion map (Fig. 34) suggest that mean extinctions are reliable. The T_{eff} -extinction degeneracy in the photometric data nonetheless mean that some extinctions are quite erroneous, although many of these were removed by the cuts applied by equations 8 to 11.
9. The extinction estimates satisfy $A_G \sim 2 \cdot E(\text{BP} - \text{RP})$. This is a consequence of the models which we are using (see Fig. 7).
10. Our extinction estimates are based on PARSEC 1.2S models with extinction assuming fixed $R_0 = 3.1$. Using a different R_0 , a different extinction law, or a different set of stellar models may lead to systematic differences compared to our current estimates.
11. We infer parameters assuming solar or near-solar metallicity (see sections 3 and 4). Our results are therefore likely to be wrong for low metallicity stars, such as in most globular clusters. The impact of this on extinction estimates for lower metallicity red clump stars can be seen in Fig. 33.
12. Stellar clusters, in particular globular clusters, are crowded regions where the integrated photometry is sometimes compromised. The BP and RP photometry are obtained by integrating over an area of $3.5 \times 2.1 \text{ arcsec}^2$. As the two Gaia fields-of-view are projected onto a common focal plane, sources can overlap even in low density regions. For crowding and other reasons, users may want to additionally filter out sources according to the “BP/RP flux excess” (see Evans et al. 2018).
13. Parallaxes are used to estimate A_G , $E(\text{BP} - \text{RP})$, \mathcal{L} , and \mathcal{R} , by giving a distance somewhat naively as $1/\varpi$ (see Bailer-Jones 2015; Luri et al. 2018). Sources without positive parallaxes therefore have no estimates of these parameters, and those with large fractional parallax uncertainties (σ_ϖ/ϖ) will have particularly noisy estimates of these parameters. This applies in particular to distant and/or faint stars. We recommend only using estimates for these parameters for stars with fractional parallax uncertainties of 20% or less.
14. The uncertainties in the \mathcal{L} and \mathcal{R} are most likely underestimated. The luminosity may suffer from a systematic error based on the adoption of the value of $BC_{G\odot}$ (see appendix D), although we estimate this to be within 0.1 mag. Luminosity will also be systematically underestimated for extincted stars, since we assumed extinction to be zero when inferring the absolute magnitude. As \mathcal{R} is derived directly from \mathcal{L} and T_{eff} , both of these effects also impact the radius estimates, albeit to a smaller degree (see section 5.4).

The application and implication of the above guidelines is illustrated in the following sections.

7.2. Selection of targets for interferometry

Measurements of apparent diameters of stars with ground-based interferometry play a crucial role for direct estimation of stellar temperatures (e.g. Heiter et al. 2015) or the validation of asteroseismic radii (e.g. White et al. 2013). Long-baseline optical interferometry can reliably measure angular diameters as small as

0.2 mas (e.g. Boyajian et al. 2015). Our results may be used to select potential targets for such interferometric observations. We suggest the following selection criteria:

$$\begin{aligned} \varpi/\sigma_\varpi &> 5 \\ \theta &= 2R \cdot \varpi > 0.2 \text{ mas} \end{aligned} \quad (12)$$

Priam flag 0100001 or 0100002

The cut on relative parallax uncertainty is obviously necessary in order to obtain a reliable distance estimate to infer a reasonably accurate diameter from the FLAME radius. We find 213 139 targets satisfying these criteria. As shown in Fig. 37, all of these are brighter than $G = 12$. Most of these targets are cool giants but some are main sequence stars. Since $\theta = 2R/r$ and the flux scales as $(R/r)^2 \propto \theta^2$, we expect $G = \text{const} - 5 \log_{10} \theta$, where the constant depends on T_{eff} , among other things. This scaling is confirmed by Fig. 37a. The diagonal stripes are due to the FLAME radius estimation relying on Priam temperatures which are based on a training sample with a inhomogeneous temperature distribution (see Fig. 18). Gaia DR2 is incomplete at the bright end (Evans et al. 2018), which unfortunately reduces the overlap with potential interferometric targets.

7.3. Selection of red clump candidates

The red clump is prominent in the de-reddened CMD in Fig. 19d. We suggest the following selection criteria to isolate candidates for red clump stars:

$$\begin{aligned} \varpi/\sigma_\varpi &> 5 \\ 1.2 < G_{\text{BP}} - G_{\text{RP}} - E(\text{BP} - \text{RP}) < 1.3 \\ 0.25 < M_G < 0.75 \end{aligned} \quad (13)$$

This selection produces 1 877 297 candidates. Of the 19 937 red clump candidates from Bovy et al. (2014), 19 240 are in Gaia DR2 and have $G < 17$, and 14 510 of these pass the astrometry criterion above. The cuts in intrinsic colour and absolute magnitude are then passed by 4415 known red clump stars.

7.4. Selection of solar analogue candidates

Based on the results from Fig. 27, we adopt the following selection criteria for solar analogue candidates:

$$\begin{aligned} \varpi/\sigma_\varpi &> 5 \\ |T_{\text{eff}} - 5772| &< 70 \\ 0.75 < G_{\text{BP}} - G_{\text{RP}} < 0.9 \\ 3.9 < G + 5 \log_{10} \varpi + 5 < 5.1 \\ 0.33 < G_{\text{BP}} - G < 0.40 \\ 0.45 < G - G_{\text{RP}} < 0.49 \end{aligned} \quad (14)$$

Priam flag 0100001 or 0100002

This selection results in 124 384 candidates for $G \leq 17$. However, we caution that this selection probably has significant contamination from non-solar-like stars with poorly estimated temperatures.

8. Looking ahead to the third Gaia data release

The broad band fluxes used in this paper were derived from Gaia’s low resolution spectrograph BP/RP. The full spectra are not made available in Gaia DR2 due to insufficient calibration

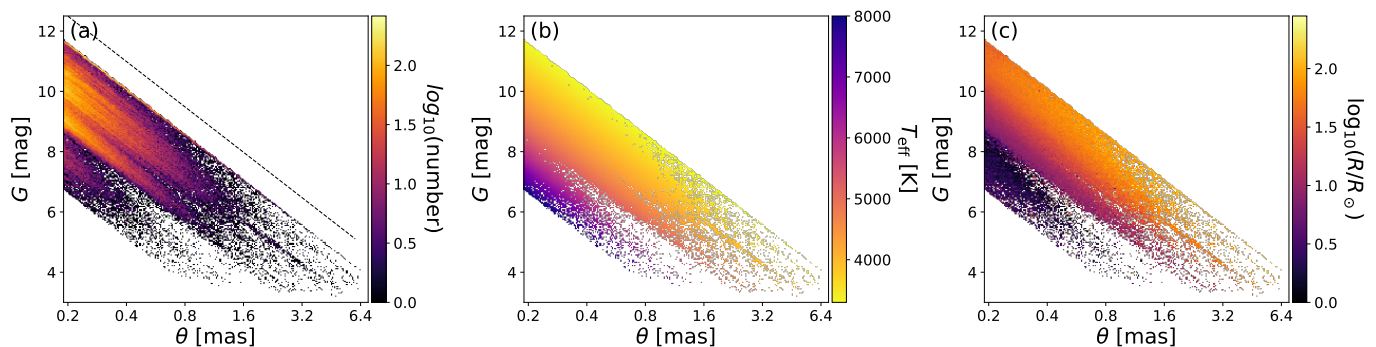


Fig. 37. Selection of target candidates for interferometry colour-coded by (a) number of stars, (b) Priam estimate of T_{eff} , and (c) FLAME estimate of radius. The stellar angular diameter θ is plotted on a log scale. We find 213 139 candidates with angular diameter $\theta > 0.2$ mas, 95 794 candidates with $\theta > 0.3$ mas, and 52 196 candidates with $\theta > 0.4$ mas. The black dashed line in panel (a) corresponds to $G = \text{const} - 5 \log_{10} \theta$.

at this stage in the data processing. For the next data release – Gaia DR3 – we plan to infer more detailed and more precise astrophysical parameters using these spectra.¹⁹ This will be done using further algorithms within the astrophysical parameter analysis system (Apsis), of which the algorithms Priam and FLAME discussed in the present paper are just a small part. For details of Apsis see Bailer-Jones et al. (2013).

The full BP/RP spectrophotometry permit estimates of both the effective temperature and the extinction without the need to use parallaxes. Simulations show that these spectra should also allow good estimates of $[\text{Fe}/\text{H}]$ and $\log g$ (Bailer-Jones 2010, 2011; Liu et al. 2012). A separate algorithm will use the spectra together with the parallaxes to estimate T_{eff} , A_G , $[\text{Fe}/\text{H}]$, and $\log g$ together with luminosity and distance, self-consistently. This should provide a more reliable distance estimate than using only the parallax (e.g. Astraatmadja & Bailer-Jones 2016), especially for sources beyond a few kpc. The radius estimates will then be more precise, and using the $\log g$ estimate we will also be able to infer mass. Using evolutionary tracks we plan also to release estimates of stellar ages for some types of stars.

Independent estimates of stellar parameters for bright stars will be possible using the high resolution radial velocity spectrograph (Gaia Collaboration et al. 2016), which gives information sensitive to T_{eff} , $[\text{M}/\text{H}]$, $[\alpha/\text{Fe}]$, and $\log g$ in the region 845–872 nm (Recio-Blanco et al. 2016). Further algorithms in Apsis will be dedicated to exploring ultra cool dwarfs (Sarro et al. 2013), emission line stars, and unresolved binary stars.

In the future we will no longer have to treat all sources as single stars. The Discrete Source Classifier in Apsis will classify sources using not only BP/RP (Bailer-Jones et al. 2008), but also the astrometry and apparent magnitude. Quasars and unresolved galaxies identified in this way will be treated by source-specific algorithms (Delchambre 2018; Bellas-Velidis et al. 2012) to derive redshift, morphology type, etc. In addition to classifying source-by-source, we also plan some global analyses to identify sources which don’t fit into our supervised classification schemes (e.g. Fustes et al. 2013), and to do large scale statistical cluster analyses to find empirical relations between sources. How much of this can be released in Gaia DR3 depends in part on the quality of the data and calibrations at the next stage of the data processing.

9. Summary

We have presented the methods used for estimating stellar parameters and line-of-sight extinctions in Gaia DR2, as well as an analysis and validation of the results. The parameter estimates are based on very limited input data, namely the parallax and the integrated photometry in three bands, G , G_{BP} , and G_{RP} . More detailed and accurate parameters should be released in Gaia DR3 once the BP/RP spectrophotometry and RVS spectra can be used.

Broadly speaking, we can estimate effective temperature T_{eff} with an accuracy of about 324 K in the range 3000K to 10 000K. For solar analogues and Gaia benchmark stars (Heiter et al. 2015), we achieve RMS errors as low as 75K and 230K, respectively. Our test and training samples were drawn from the same parent distribution, which are not necessarily representative of all stellar populations. For the same reason, there are some systematic misestimations of T_{eff} , e.g. for sources with very low or very high extinctions (see Fig. 11e and Fig. 12). Likewise, there appear to be systematic trends with the actual temperature (Fig. 11c), the colour (Fig. 11f) and with metallicity (Fig. 24b). These figures attempt to quantify these systematics, but they are not included in the 324K uncertainty estimates which, by definition, quantify only *random* errors. The reported 16th and 84th percentiles appear to be consistent with differences to literature estimates when also accounting for literature uncertainty estimates.

The line-of-sight extinction A_G and the reddening $E(\text{BP} - \text{RP})$ are estimated with global uncertainties of 0.46 mag and 0.23 mag, respectively (section 6.5). Better estimates can be achieved for red clump stars (section 6.6). Note that A_G is the extinction in the G-band rather than an extinction parameter, so also depends on the spectral energy distribution (and thus T_{eff}) of the star. Thus a given amount of dust can correspond to different values of A_G , depending on the type of star. Given only three broad optical bands as input data, there are obviously strong degeneracies; we have explored the systematics these can introduce into our extinction estimates. After applying quality cuts to remove outliers, there is no evidence for further biases. Nevertheless, with such large random errors A_G and $E(\text{BP} - \text{RP})$ are of limited use for individual stars. However, A_G and $E(\text{BP} - \text{RP})$ can be used statistically on a set of stars, for example to apply a dust correction in the colour-magnitude diagram. Given the degeneracy, for our T_{eff} estimations and our subsequent estimations of bolometric luminosity \mathcal{L} and radius \mathcal{R} , we have assumed the sources have zero (or at least low) extinction.

¹⁹ Initial results with preliminary BP/RP spectra in an empirically-trained algorithm show very promising results when comparing to the literature, not only for T_{eff} , but also for $[\text{Fe}/\text{H}]$ and $\log g$.

Adopting a bolometric correction offset determined empirically, we have estimated \mathcal{L} to an accuracy of about 15% and \mathcal{R} to about 10% (RMS errors), again without significant systematics.

Given the limited input data, we necessarily rely on a number of assumptions and simplifications. We list some known limitations of our results in section 7.1. These must be considered when using our data products. We recommend that only our clean T_{eff} sample be used (appendix B). For better estimates of extinction, users may want to only use stars with some maximum fractional parallax uncertainty (see Fig. 19 for an example of this).

Finally, we emphasise again that the objective of this work was to provide stellar parameter estimates using Gaia data only. Substantially better results are likely achievable when combining with other data, such as GALEX (Morrissey et al. 2007), PanSTARRS (Chambers et al. 2016) or WISE (Cutri et al. 2014). McDonald et al. (2017) and Stevens et al. (2017) have attempted that already with Gaia DR1 data, although they faced severe problems with cross-matching the different catalogues due to the high spatial resolution of the Gaia catalogue. Great care must be exercised when using multi-catalogue spectral energy distributions resulting from such cross-matches, since the passbands are not always well defined for some photometric systems (e.g., APASS; Henden et al. 2016).

Although limited in precision and accuracy, our results should nonetheless be useful as the largest, all-sky catalogue of homogeneously-inferred stellar parameters published to date, and the first to use parallaxes on a large scale.

Acknowledgements. For their constructive comments on the manuscript we thank Carine Babusiaux, Anthony Brown, Ron Drimmel, Yves Frémat, Carme Jordi, Jan Rybizki, Antonella Vallenari, and the anonymous referee. We thank Floor van Leeuwen for providing membership lists of stellar clusters in Gaia DR2. This work is based on data from the European Space Agency (ESA) mission *Gaia* (<https://www.cosmos.esa.int/gaia>), processed by the *Gaia* Data Processing and Analysis Consortium (DPAC, <https://www.cosmos.esa.int/web/gaia/dpac/consortium>). Funding for the DPAC has been provided by national institutions, in particular the institutions participating in the *Gaia* Multilateral Agreement. Funding specifically for the DPAC work in this paper has been provided by the DLR (German space agency) via grants 50 QG 0602, 50 QG 1001, and 50 QG 1403. AJK acknowledges support by the Swedish National Space Board (SNSB). This research has made extensive use of IPython (Pérez & Granger 2007), matplotlib (Hunter 2007), and Vaex (Breddels 2017).

References

- Alam, S., Albaret, F. D., Allende Prieto, C., et al. 2015, *ApJS*, 219, 12
- Astraatmadja, T. L. & Bailer-Jones, C. A. L. 2016, *ApJ*, 833, 119
- Bailer-Jones, C. A. L. 2010, *MNRAS*, 403, 96
- Bailer-Jones, C. A. L. 2011, *MNRAS*, 411, 435
- Bailer-Jones, C. A. L. 2015, *PASP*, 127, 994
- Bailer-Jones, C. A. L., Andrae, R., Arcay, B., et al. 2013, *A&A*, 559, A74
- Bailer-Jones, C. A. L., Smith, K. W., Tiede, C., Sordo, R., & Vallenari, A. 2008, *MNRAS*, 391, 1838
- Basu, S., Grundahl, F., Stello, D., et al. 2011, *ApJ*, 729, L10
- Bellas-Velidis, I., Kontizas, M., Dapergolas, A., et al. 2012, *Bulgarian Astronomical Journal*, 18, 020000
- Bishop, C. M. 2006, *Pattern Recognition and Machine Learning* (Springer)
- Bourges, L., Mella, G., Lafrasse, S., et al. 2017, *VizieR Online Data Catalog*, 2346
- Bovy, J., Nidever, D. L., Rix, H.-W., et al. 2014, *ApJ*, 790, 127
- Boyajian, T., von Braun, K., Feiden, G. A., et al. 2015, *MNRAS*, 447, 846
- Boyajian, T. S., von Braun, K., van Belle, G., et al. 2013, *ApJ*, 771, 40
- Breddels, M. A. 2017, in *IAU Symposium*, Vol. 325, *IAU Symposium*, 299–304
- Bressan, A., Marigo, P., Girardi, L., et al. 2012, *MNRAS*, 427, 127
- Cardelli, J. A., Clayton, G. C., & Mathis, J. S. 1989, *ApJ*, 345, 245
- Casagrande, L., Schoenrich, R., Asplund, M., et al. 2011, *VizieR Online Data Catalog*, 353
- Castellani, V., Degl'Innocenti, S., Prada Moroni, P. G., & Tordiglione, V. 2002, *MNRAS*, 334, 193
- Castelli, F. & Kurucz, R. L. 2003, in *IAU Symposium*, Vol. 210, *Modelling of Stellar Atmospheres*, ed. N. Piskunov, W. Weiss, & D. Gray
- Chambers, K. C., Magnier, E. A., Metcalfe, N., et al. 2016, *ArXiv e-prints* 1612.05560
- Chaplin, W. J., Basu, S., Huber, D., et al. 2014, *VizieR Online Data Catalog*, 221
- Creevey, O. L., Metcalfe, T. S., Schultheis, M., et al. 2017, *VizieR Online Data Catalog*, 360
- Cutri, R. M., Wright, E. L., Conrow, T., et al. 2014, *VizieR Online Data Catalog*, 2328
- de Bruijne, J. H. J. 2012, *Ap&SS*, 341, 31
- Delchambre, L. 2018, *MNRAS*, 473, 1785
- Deming, W. 1943, *Statistical Adjustment of Data*, Dover books on elementary and intermediate mathematics (Dover Publ. Incorporated)
- Deng, N., Tian, Y., & Zhang, C. 2012, *Support Vector Machines: Optimization Based Theory, Algorithms, and Extensions*, 1st edn. (Chapman & Hall/CRC)
- Dowson, D. & Wragg, A. 2006, *IEEE Trans. Inf. Theor.*, 19, 689
- Evans, D., Riello, M., De Angeli, F., et al. 2018, *A&A*
- Fuller, W. 2009, *Measurement Error Models*, Wiley Series in Probability and Statistics (Wiley)
- Fustes, D., Manteiga, M., Dafonte, C., et al. 2013, *A&A*, 559, A7
- Gaia Collaboration, Babusiaux, C., & et al. 2018a, *A&A*
- Gaia Collaboration, Brown, A., Vallenari, A., Prusti, T., & de Bruijne, J. 2018b, *A&A*
- Gaia Collaboration, Prusti, T., de Bruijne, J. H. J., et al. 2016, *A&A*, 595, A1
- Geurts, P., Ernst, D., & Wehenkel, L. 2006, *Mach. Learn.*, 63, 3
- Gustafsson, B., Edvardsson, B., Eriksson, K., et al. 2008, *A&A*, 486, 951
- Heiter, U., Jofré, P., Gustafsson, B., et al. 2015, *A&A*, 582, A49
- Henden, A. A., Templeton, M., Terrell, D., et al. 2016, *VizieR Online Data Catalog*, 2336
- Huber, D., Silva Aguirre, V., Matthews, J. M., et al. 2014, *ApJS*, 211, 2
- Hunter, J. D. 2007, *Computing In Science & Engineering*, 9, 90
- Jordi, C., Gebran, M., Carrasco, J. M., et al. 2010, *A&A*, 523, A48
- Kleinman, S. J., Kepler, S. O., Koester, D., et al. 2013, *ApJS*, 204, 5
- Kordopatis, G., Gilmore, G., Steinmetz, M., et al. 2013, *AJ*, 146, 134
- Lallement, R., Vergely, J.-L., Valette, B., et al. 2014, *A&A*, 561, A91
- Ligi, R., Creevey, O., Mourard, D., et al. 2016, *VizieR Online Data Catalog*, 358
- Lindgren, L., Hernández, J., Bombrun, A., et al. 2018, *A&A*
- Liu, C., Bailer-Jones, C. A. L., Sordo, R., et al. 2012, *MNRAS*, 426, 2463
- Luo, A.-L., Zhao, Y.-H., Zhao, G., et al. 2015, *Research in Astronomy and Astrophysics*, 15, 1095
- Luri, X., Brown, A., Sarro, L., et al. 2018, *A&A*
- Martell, S. L., Sharma, S., Buder, S., et al. 2017, *MNRAS*, 465, 3203
- McDonald, I., Zijlstra, A. A., & Watson, R. A. 2017, *MNRAS*, 471, 770
- Morrissey, P., Conrow, T., Barlow, T. A., et al. 2007, *ApJS*, 173, 682
- O'Donnell, J. E. 1994, *ApJ*, 422, 158
- Pandey, A. K., Upadhyay, K., Nakada, Y., & Ogura, K. 2003, *A&A*, 397, 191
- Pérez, F. & Granger, B. E. 2007, *Computing in Science and Engineering*, 9, 21
- Pickles, A. J. 1998, *PASP*, 110, 863
- Ramírez-Agudelo, O. H., Sana, H., de Koter, A., et al. 2017, *A&A*, 600, A81
- Recio-Blanco, A., de Laverny, P., Allende Prieto, C., et al. 2016, *A&A*, 585, A93
- Riello, M., De Angeli, F., Evans, D., et al. 2018, *A&A*
- Rodrigues, T. S., Girardi, L., Miglio, A., et al. 2014, *MNRAS*, 445, 2758
- Ruiz-Dern, L., Babusiaux, C., Arenou, F., Turon, C., & Lallement, R. 2017, *ArXiv e-prints* 1710.05803
- Sarro, L. M., Berihuete, A., Carrión, C., et al. 2013, *A&A*, 550, A44
- Sarro, L. M., Debusscher, J., De Ridder, J., et al. 2016, *Technical Note GAIA-C7-TN-SVO-LSB-015*
- Sartoretti, P., Katz, D., Cropper, M., et al. 2018, *A&A*
- Schlaflly, E. F., Green, G., Finkbeiner, D. P., et al. 2015, *ApJ*, 799, 116
- Schlegel, D. J., Finkbeiner, D. P., & Davis, M. 1998, *ApJ*, 500, 525
- Simón-Díaz, S., Castro, N., García, M., Herrero, A., & Markova, N. 2011, *Bulletin de la Société Royale des Sciences de Liège*, 80, 514
- Simón-Díaz, S., Godart, M., Castro, N., et al. 2017, *A&A*, 597, A22
- Sirko, E., Goodman, J., Knapp, G. R., et al. 2004, *AJ*, 127, 899
- Soubiran, C., Lécampion, J., & Chemin, L. 2014, *Technical Note GAIA-C6-TN-LAB-CS-011-2*
- Stevens, D. J., Stassun, K. G., & Gaudi, B. S. 2017, *AJ*, 154, 259
- Tammann, G. A., Sandage, A., & Reindl, B. 2003, *VizieR Online Data Catalog*, 340
- Taylor, B. J. 2006, *AJ*, 132, 2453
- Torres, G. 2010, *AJ*, 140, 1158
- Tucci Maia, M., Ramírez, I., Meléndez, J., et al. 2016, *A&A*, 590, A32
- Vrard, M., Mosser, B., & Samadi, R. 2016, *A&A*, 588, A87
- White, T. R., Huber, D., Maestro, V., et al. 2013, *MNRAS*, 433, 1262
- Wils, P., Lloyd, C., & Bernhard, K. 2006, *MNRAS*, 368, 1757
- Zasowski, G., An, D., & Pinsonneault, M. 2015, in *Astrophysics and Space Science Proceedings*, Vol. 39, *Asteroseismology of Stellar Populations in the Milky Way*, ed. A. Miglio, P. Eggenberger, L. Girardi, & J. Montalbán, 83

Appendix A: Filtering applied to produce the Gaia DR2 catalogue

Some of the sources processed by Apsis have poor data and cannot yield useful astrophysical parameters. Likewise, our assumptions may sometimes yield invalid results. We therefore apply various filters in post-processing in order to remove some or all parameter estimates. (These filters are applied during the creation of the final catalogue.) Table A.1 lists these filters. In addition we always require complete photometry – fluxes available for all of G, BP, and RP – to produce any results, and we only processed sources with $G \leq 17.068766$. Filters applied by other parts of the processing could remove some sources entirely, regardless of the Apsis results. For more details on filtering, see the online documentation with Gaia DR2. The number of sources in the catalogue with an extant estimate for each parameter is as follows: T_{eff} : 161 497 595; A_G and $E(\text{BP} - \text{RP})$: 87 733 672; \mathcal{L} and \mathcal{R} : 76 956 778.

Table A.1. Filters applied to the Apsis results to determine whether certain parameters are excluded from Gaia DR2 for individual stars. $\sigma(T_{\text{eff}})$ is defined as half the confidence interval, i.e. half the difference between the 84th and 16th percentiles. Excluding the estimate of a parameter also excludes its uncertainty estimates. The Priam flags are defined in Table B.1.

condition	parameters excluded			
$\varpi \leq 0$	A_G	$E(\text{BP} - \text{RP})$	\mathcal{L}	\mathcal{R}
$\sigma_{\varpi}/\varpi > 0.2$			\mathcal{L}	\mathcal{R}
$T_{\text{eff}} < 3300 \text{ K}$ or $T_{\text{eff}} > 8000 \text{ K}$			\mathcal{L}	\mathcal{R}
$\sigma(T_{\text{eff}})/T_{\text{eff}} > 0.2$			\mathcal{L}	\mathcal{R}
$\sigma(\mathcal{L})/\mathcal{L} > 0.3$			\mathcal{L}	\mathcal{R}
$\mathcal{R} < 0.5 \mathcal{R}_0$			\mathcal{L}	\mathcal{R}
violation of equations (8)-(11)	A_G	$E(\text{BP} - \text{RP})$		
Priam flag > 0100002	A_G	$E(\text{BP} - \text{RP})$		

Appendix B: The Apsis flags

Various flags are written by Apsis during processing to indicate the quality of the input data and/or the results. They have the format XYABCDE, where each letter represents a decimal digit. XY=01 indicates a Priam flag, the values of which are shown in Table B.1.

Digits C and D refer to colours in the union of the T_{eff} and extinction training sets. These can be used to remove sources which are unlikely to get good results from Priam. The colour ranges for the separate models are as follows (so a colour selection could be used for the parameter of interest, instead of using these digits in the flags): For T_{eff} $G_{\text{BP}} - G$: -0.06 to 4.38 mag , $G - G_{\text{RP}}$: -0.15 to 2.08 mag . For extinction: $G_{\text{BP}} - G$: -0.12 to 4.66 mag , $G - G_{\text{RP}}$: -0.20 to 1.69 mag .

To get a clean sample of T_{eff} estimates, use only sources with Priam flag values equal to 0100001, 0100002, 0110001, 0110002, 0120001, or 0120002, i.e. A and E can have any value, but B, C, and D are zero. When using T_{eff} for astrophysical analyses, we recommend that this clean sample be used.

For A_G and $E(\text{BP} - \text{RP})$ estimates, the filtering on best Priam flag values has already been applied during the catalog production for Gaia DR2. The user may want to make further cuts to only retain sources with low fractional parallax uncertainties.

After the filtering described in Table A.1, only one flag corresponding to FLAME is left in the catalogue (the one beginning with 02), so can be ignored. Since FLAME results depend on

T_{eff} , we recommend to only use FLAME results for the clean T_{eff} sample.

Appendix C: Uncertainty estimates for A_G and $E(\text{BP} - \text{RP})$

In section 6.6, we estimate the uncertainties in A_G for red clump stars from Bovy et al. (2014) by comparing our estimate of A_G to the observable $G + 5 \log_{10} \varpi + 5$ (which is equal to $M_G + A_G$). Likewise, we also compare $E(\text{BP} - \text{RP})$ to the observed colour $G_{\text{BP}} - G_{\text{RP}}$. In these cases, both variables, call them x and y , have uncertainties, so a standard least-squares regression would lead to systematically wrong results for the slopes and intercepts in Fig. 33 (e.g. Fuller 2009, section 1.1.1 therein). For each y_n (the observable), the corresponding uncertainty σ_n can be obtained by the usual propagation of uncertainties in the G-band flux and the parallax. The uncertainty σ_x in x and the intercept are our desired estimates. These tell us the uncertainties in A_G and $E(\text{BP} - \text{RP})$, respectively, and whether we are consistent with the expected absolute magnitude and intrinsic colour of the red clump.

When both x and y have uncertainties, then in order to obtain an unbiased estimate of σ_x , we use a modification of the Deming formalism (e.g. Deming 1943). We introduce the true \hat{x}_n and true \hat{y}_n , which satisfy the linear relation

$$\hat{y}_n = c_0 + \hat{x}_n. \quad (\text{C.1})$$

The intercept c_0 is the absolute magnitude of the red clump stars for A_G or the intrinsic colour for $E(\text{BP} - \text{RP})$, which remains a free fit parameter. We set the slope to $c_1 = 1$, since Fig. 33b and d have already established an approximate one-to-one relation between x and y and we now seek the uncertainty of x under this relation. We then estimate the true \hat{x}_n , the intercept c_0 and the uncertainty σ_x by minimising

$$\chi^2 = 2N \log \sigma_x + \sum_{n=1}^N \left[\left(\frac{y_n - c_0 - \hat{x}_n}{\sigma_n} \right)^2 + \left(\frac{x_n - \hat{x}_n}{\sigma_x} \right)^2 \right]. \quad (\text{C.2})$$

Note the first term which ensures that the likelihood function is normalised, while we fit for the unknown uncertainty σ_x . This minimisation has analytic results

$$\hat{x}_n = x_n + \frac{y_n - c_0 - x_n}{1 + \sigma_n^2 / \sigma_x^2} \quad \forall n = 1, \dots, N \quad (\text{C.3})$$

and

$$c_0 = \frac{\sum_{n=1}^N \frac{y_n - x_n}{\sigma_n^2 + \sigma_x^2}}{\sum_{n=1}^N \frac{1}{\sigma_n^2 + \sigma_x^2}}. \quad (\text{C.4})$$

Unfortunately, there is no analytic solution for σ_x . However, a numerical solution can be found easily.

Appendix D: Bolometric correction scale

The bolometric correction used to compute the luminosity \mathcal{L} is calculated on a grid of synthetic stellar spectra for varying values of T_{eff} , $\log g$, $[\text{Fe}/\text{H}]$, and $[\alpha/\text{Fe}]$. While the variation of the bolometric correction with stellar parameters can be easily evaluated considering any filter band pass, the absolute value can only be derived if we know the absolute magnitude M_G for one source with known bolometric flux and distance. The Sun is the obvious choice. From hereon, we refer to this as the offset of the

Table B.1. Definition of Priam processing flags, which have format 01ABCDE.

position	value	meaning
A	0	parallax value is strictly positive ($\varpi > 0$)
	1	parallax value is non-positive ($\varpi \leq 0$) such that extinction estimate does not work
	2	while $\varpi > 0$ the parallax error is $\sigma_{\varpi} > 1$ mas
B	0	both colours are close to the standard locus
	1	below standard locus, i.e., $G_{BP} - G > 0.1$ and $(G - G_{RP}) < (G_{BP} - G - 0.1)^{0.4} - 0.3$
	2	above standard locus, i.e., $(G - G_{RP}) > (2.5 \cdot ((G_{BP} - G) + 0.02))$ or $(G - G_{RP}) > (0.5 \cdot ((G_{BP} - G) - 1.0) + 1.1)$
C	0	$G - G_{RP}$ colour is inside union of T_{eff} and extinction training sets
	1	$G - G_{RP}$ colour is smaller than union of T_{eff} and extinction training sets
	2	$G - G_{RP}$ colour is larger than union of T_{eff} and extinction training sets
D	0	$G_{BP} - G$ colour is inside union of T_{eff} and extinction training sets
	1	$G_{BP} - G$ colour is smaller than union of T_{eff} and extinction training sets
	2	$G_{BP} - G$ colour is larger than union of T_{eff} and extinction training sets
E	1	input data was gold photometry
	2	input data was silver photometry

bolometric correction, and this is the value of a_0 in equation 7 for the T_{eff} range 4 000 – 8 000 K.

Adopting the previously-mentioned IAU resolution 2015 B2, the Sun’s bolometric magnitude is $M_{\text{bol}\odot} = 4.74$ mag. Given its distance and its measured V -band magnitude, $V_{\odot} = -26.76 \pm 0.03$, the absolute magnitude $M_{V\odot} = 4.81$ is calculated and the BC_V is derived: $BC_V = 4.74 - 4.81 = -0.07$ mag (Torres 2010). However, we do not have a measure of G_{\odot} , and so we cannot apply these equations directly to determine BC_G . Thus to derive the offset to the bolometric correction scale there are four options: (1) estimate G_{\odot} from stellar models; (2) use a V to G conversion; (3) externally calibrate using stars with accurately measured luminosities and radii; (4) use solar twins to measure M_G (see section 6). We chose to adopt solution (3) and this is described in detail here. It’s also appropriate given that our T_{eff} estimates are based on empirically trained models.

We derive our bolometric correction offset by comparing our overall estimates of luminosity and radius with those from other studies. This works provided the stars in question have accurately determined extinctions (often taken to be zero). Net offsets can indicate a problem with the offset of the bolometric correction (in our study or in the other studies, or both). We perform this comparison on three samples of stars: (1) the Casagrande et al. (2011) analysis of the Geneva Copenhagen Survey data; (2) the JMMC Catalogue of Stellar Diameters (Bourges et al. 2017); (3) an asteroseismic sample of giant stars from Vrad et al. (2016). For these samples we also selected those stars where Priam $\sigma_{T_{\text{eff}}}/T_{\text{eff}} < 3\%$ and Gaia $\sigma_{\varpi}/\varpi < 5\%$.

Casagrande et al. (2011) provide bolometric flux and T_{eff} in their catalogue. Using these along with the Gaia parallaxes we calculated stellar radii and luminosities. From this sample we selected the stars within 100 pc ($N = 307$ stars in the sample), 200 pc ($N = 809$) and 300 pc ($N = 895$) of the Sun, and we imposed $7 < G < 10$. We first compared the Priam T_{eff} with theirs, and by adding an offset to compensate for the differences in our T_{eff} we rederived our radii. This was done to isolate the effect of the BC_G . Then we adjusted $BC_{G\odot}$ until we minimized the mean difference between our results (luminosities and rederived radii) and theirs. This resulted in $BC_{G\odot} = +0.10, +0.09, +0.09$ mag for the three distance cuts respectively.

The JMMC catalogue (Bourges et al. 2017) predicts angular diameters from magnitudes and colours; this is the so-called surface-brightness relation. It is calibrated using interferometric

measurements of stellar diameters. We performed the same analysis on this catalogue for stars within 100 pc ($N = 1\,182$), 200 pc ($N = 5\,427$), and 300 pc ($N = 6\,332$). By minimizing the mean differences between the radii we derived a $BC_{G\odot}$ of $+0.00, +0.01$, and $+0.01$ mag for the three distance cuts respectively.

The third catalogue we used consists of thousands of giants in the *Kepler* field analysed using asteroseismology (Vrad et al. 2016). Our validation sample comprises 3355 stars. In this case we can not assume that extinction is zero or negligible. The effect of the bolometric correction offset and extinction for deriving \mathcal{L} is degenerate. Thus we are required to assume a mean extinction for these stars if we wish to estimate $BC_{G\odot}$. We adopted $A_V = 0.25 \pm 0.10$ mag (see for example Rodrigues et al. 2014; Zasowski et al. 2015). We then used an $A_G - A_V$ conversion to fix $A_G = +0.21$ mag in our subsequent analysis. By repeating the analysis described above, we obtained $BC_{G\odot} = +0.04$ mag as the best overall agreement between our results and those from Vrad et al. (2016).

Following these analyses, along with subsequent validation (section 6.8), we conclude that the uncertainty in the offset of the bolometric correction is about 0.10 mag, and we somewhat arbitrarily set the offset to fall within the extremes that we found here, and define it as $BC_{G\odot} = +0.060$ mag. This is the value of the a_0 coefficient for the temperature range 4 000 – 8 000 K in Table 4. This result implies $M_{G\odot} = 4.68$ mag and consequently $(G - V)_{\odot} = -0.13$ mag. This value is corroborated by the results on solar analogues (section 6.4).

Appendix E: Estimation of cluster extinction

As our extinction and reddening estimates are very noisy and also constrained to be non-negative, their combination (for parameter estimation) becomes non-trivial. Here we first outline how to use our results, using the example of estimating the extinction in a star cluster. Second, we show that the sample mean is generally a poor estimator that suffers from strong biases. Third, we use the clusters to obtain another global uncertainty estimate for our extinctions (independent of section 6.5).

Suppose we have estimated A_G for N cluster members, whereby each estimate has a common uncertainty σ . (We will not use out inferred confidence interval – 16th and 84th percentiles – for each extinction.) Suppose further that the intrinsic scatter in the true extinctions is negligible compared to this un-

certainty.²⁰ Then the true (but unknown) extinctions are all equal to the cluster extinction, μ . We want to infer μ and σ from the N measurements. The likelihood $P(A_G|\mu, \sigma)$ which makes the fewest assumptions in this case is the Gaussian. If A_G is additionally restricted to a finite range (as is the case for our EXTRATREES outputs), then the least-informative likelihood distribution is a Gaussian truncated over this range (Dowson & Wragg 2006).²¹ This we can write (properly normalized) as

$$p(A_G|\mu, \sigma) = \begin{cases} \frac{\frac{1}{\sigma\sqrt{2\pi}} \exp\left[-\frac{1}{2}\left(\frac{A_G-\mu}{\sigma}\right)^2\right]}{\frac{1}{2}\left[\operatorname{erf}\left(\frac{A_G^{\max}-\mu}{\sqrt{2}\sigma}\right) + \operatorname{erf}\left(\frac{\mu-A_G^{\min}}{\sqrt{2}\sigma}\right)\right]} & \text{for } A_G \in [A_G^{\min}, A_G^{\max}] \\ 0 & \text{otherwise} \end{cases}, \quad (\text{E.1})$$

where

$$\operatorname{erf}(z) = \frac{2}{\sqrt{\pi}} \int_0^z e^{-t^2} dt. \quad (\text{E.2})$$

Throughout this appendix we fix $A_G^{\min} = 0$ and $A_G^{\max} = 3.609$ mag, which is the A_G range in the Priam training sample ($A_0 \in [0, 4]$ mag).

For the set of N cluster members, the total likelihood is just the product of the single-star likelihoods. Note that due to the limitation $A_G \in [0, 3.609]$ the normalisation constant of the likelihood now depends on the cluster extinction μ (and not only on σ). For this reason, there is no analytic solution for either of the parameters. In particular, the sample mean is no longer a useful estimator for the cluster extinction μ , which is not the mean of the truncated Gaussian (it is the mode, provided it lies within $[A_G^{\min}, A_G^{\max}]$). We illustrate this with a simulation in which we draw a number of samples from a truncated Gaussian with specified true extinction μ and fixed $\sigma = 0.46$ mag and compare the sample mean, $\langle A_G \rangle$, to the true extinction of the simulation. As is obvious from Fig. E.1, if the true extinction approaches the lower or upper limit, the sample mean becomes biased. Only for clusters with intrinsic extinctions between about 1.3 mag and 2.4 mag can we expect the sample mean to be a reliable estimator, i.e. when the intrinsic extinction is about 3σ or more away from the lower and upper limits. For low-extinction clusters, the bias of the sample mean will be largest and of the same order as σ for our A_G estimates, i.e. we may obtain a 0.4 mag or larger sample mean $\langle A_G \rangle$ for clusters whose expected intrinsic extinction is zero. We emphasise that this bias does *not* diminish if we have more cluster members, as is also clear from Fig. E.1.

Since the sample mean is no longer a useful estimator in general, we must use the likelihood from equation E.1 in order to estimate parameters. We find the maximum of the likelihood (Bayesians may add priors).²² In Table E.1 we provide our estimates for the 46 clusters from Gaia Collaboration et al.

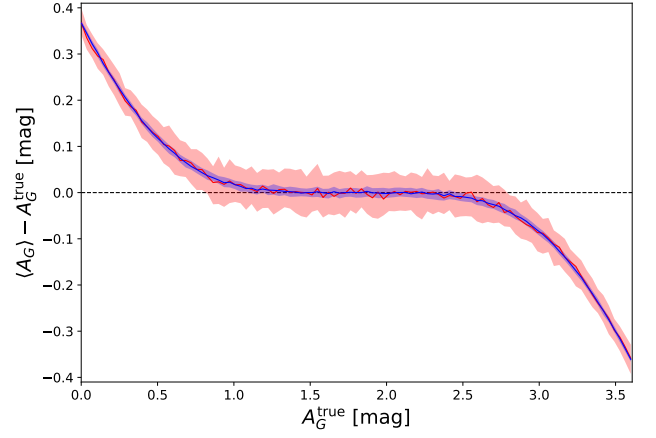


Fig. E.1. Simulation showing how the sample mean is a biased estimator of the cluster extinction when using 100 cluster member stars (red) and 2000 members (blue) with $\sigma = 0.46$ mag. Shaded areas show the central 68% confidence interval estimated from 101 simulations.

(2018a). Fig. E.2 shows the likelihood function over μ and σ for the Pleiades, Praesepe, Hyades and NGC884. For Praesepe and the Pleiades, the estimated cluster extinctions agree very well with the literature values. Emphasizing the point from Fig. E.1, the sample mean extinction for Praesepe is $\langle A_G \rangle = 0.4$ mag, whereas the maximum likelihood estimate is actually $\hat{\mu} = 0$ mag (see Table E.1), which compares favourably with the literature estimate of 0.03 mag used in section 6.7. For the Pleiades, the sample mean is 0.48 mag while the maximum likelihood estimate is 0.11 mag (cf. literature estimate of 0.12 mag). We obtain $\hat{\sigma} = 0.59$ mag and 0.54 mag for Praesepe and Pleiades respectively, which are larger than our global uncertainty estimate of 0.46 mag from section 6.5. In the case of the Hyades we clearly overestimate the cluster extinction with $\hat{\mu} = 0.21$ mag while $\hat{\sigma} = 0.42$ mag is slightly below our global uncertainty estimate. (Note from Fig. E.2 that these two quantities are negatively correlated when approaching the lower boundary.) We suspect this to be shot noise from the finite number of cluster members with A_G measurements. Indeed, simulating 100 Hyades-like samples, each with true $\mu = 0.01$ mag, true $\sigma = 0.46$ mag, and 369 stars, we observe poor estimates in 8% of the cases. It may come as a surprise that 369 stars is not necessarily sufficient to reliably estimate the cluster extinction and the scatter. The explanation is that for a low-extinction cluster such as the Hyades, the truncation of the Gaussian is dominant. We are trying to infer a pathological distribution, so the estimate of the mode of the distribution, μ , is more sensitive to the set of samples than is the sample mean. As an example of a cluster with higher extinction, the maximum-likelihood estimate of NGC884 (panels d and h of Fig. E.2) also agrees reasonably well with the literature ($E(B - V) = 0.58$ mag from Pandey et al. 2003, which corresponds to $A_0 \simeq 1.8$ mag). Nevertheless, although our maximum-likelihood estimates of the cluster extinctions are largely consistent with the expected values, the random errors are still far too large for detailed studies of Hertzsprung-Russell diagrams in clusters.

Finally, we can see from Table E.1 that the maximum-likelihood estimates of σ vary quite considerably, sometimes being below and sometimes above our global uncertainty estimate of 0.46 mag from section 6.5. Unsurprisingly, the estimation of

²⁰ As A_G also depends on the spectral energy distribution of a star, this is true only for low-extinction clusters. Taking all PARSEC models with $\mathcal{Z} = \mathcal{Z}_\odot = 0.0152$, $A_0 = 2$ mag and $\log_{10}(\text{age/yr}) = 9.7$, then A_G ranges from 1.10 to 1.68 mag and $E(\text{BP} - \text{RP})$ ranges from 0.73 to 0.84 mag.

²¹ The least-informative distribution is derived from a maximum entropy argument, as used in section 6.5 to arrive at the exponential distribution for high Galactic latitudes. The maximum entropy distribution is different in the present case because we now impose a mode μ and a variance σ^2 , which are the parameters of our model we want to find.

²² The maximum likelihood estimate $\hat{\mu}$ can be negative, but we truncate this to zero on the grounds that true cluster extinctions cannot be negative (this is just a prior). Highly extinct clusters could have true

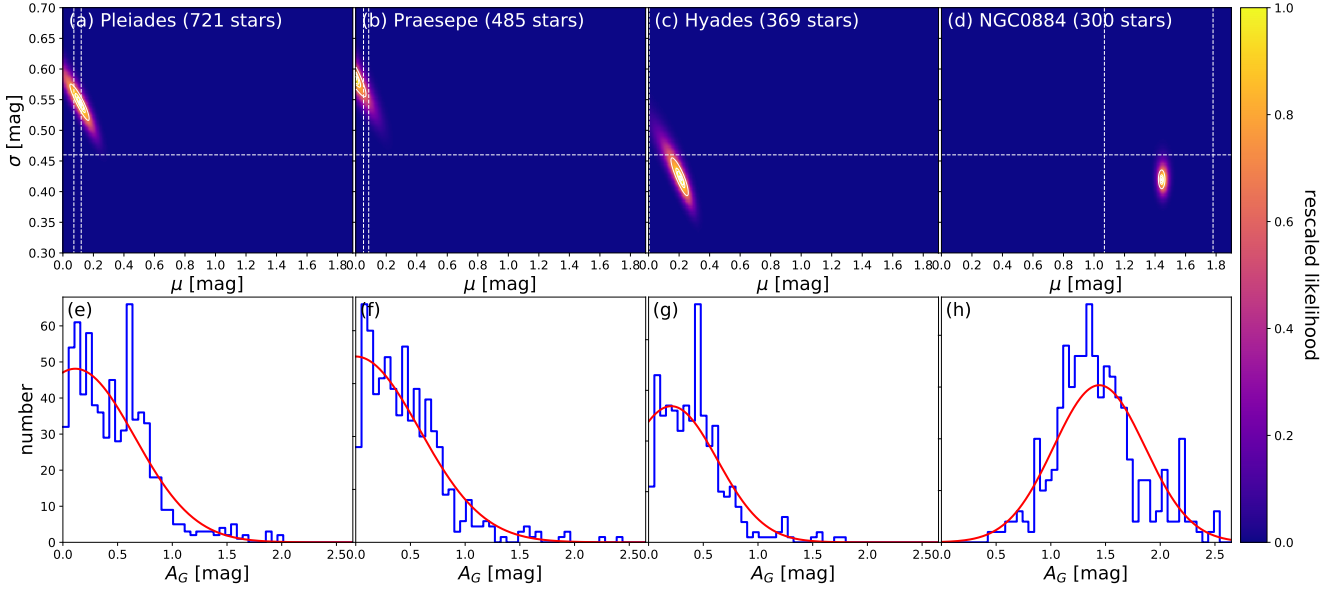


Fig. E.2. Estimating cluster extinctions for Pleiades (a,e), Praesepe (b,f), Hyades (c,g) and NGC884 (d,h). The top row shows likelihood maps of cluster extinction μ and global uncertainty estimate σ . Contours show 68%, 90%, 95% and 99% confidence regions. The horizontal dashed line indicates our global uncertainty estimate of 0.46 mag from section 6.5. Vertical dashed lines are $A_G \sim (0.6 - 1.0) \cdot A_0$ (Jordi et al. 2010, Fig. 17 therein) for literature estimates of $A_0 \sim 3.1 \cdot E(B - V)$ from Pandey et al. (2003). The bottom row shows, for each cluster, the histogram of estimated A_G (black) and the maximum-likelihood estimate of the truncated Gaussian (red).

cluster extinctions works better for some samples than for others.

Table E.1. Estimates of the cluster extinction using the sample mean $\langle A_G \rangle$ (which is biased) and the maximum likelihood (ML) estimates of μ , as well as the global uncertainty σ . Clusters are sorted with descending number of member stars. Nearby clusters within 250pc are marked in bold face. Cluster memberships are taken from Gaia Collaboration et al. (2018a).

name	no. of stars	ML estimates		
		$\langle A_G \rangle$ mag	$\hat{\mu}$ mag	$\hat{\sigma}$ mag
NGC3532	1217	0.293	0.000 ^{+0.005} _{-0.000}	0.406 ^{+0.007} _{-0.009}
NGC2437	962	0.538	0.503 ^{+0.012} _{-0.013}	0.309 ^{+0.011} _{-0.008}
NGC2516	894	0.373	0.083 ^{+0.042} _{-0.052}	0.427 ^{+0.025} _{-0.020}
NGC2682	724	0.371	0.000 ^{+0.025} _{-0.000}	0.479 ^{+0.008} _{-0.020}
Pleiades	721	0.478	0.113 ^{+0.056} _{-0.073}	0.544 ^{+0.034} _{-0.027}
NGC2168	709	0.629	0.619 ^{+0.010} _{-0.012}	0.283 ^{+0.009} _{-0.008}
NGC6475	612	0.373	0.165 ^{+0.042} _{-0.055}	0.381 ^{+0.031} _{-0.020}
Praesepe	485	0.464	0.000 ^{+0.078} _{-0.000}	0.585 ^{+0.005} _{-0.047}
IC4651	474	0.506	0.360 ^{+0.037} _{-0.047}	0.423 ^{+0.031} _{-0.022}
NGC0188	450	0.585	0.504 ^{+0.026} _{-0.032}	0.402 ^{+0.025} _{-0.018}
NGC2360	421	0.444	0.085 ^{+0.055} _{-0.074}	0.516 ^{+0.030} _{-0.036}
Stock2	410	0.802	0.779 ^{+0.021} _{-0.022}	0.394 ^{+0.019} _{-0.016}
NGC2447	377	0.267	0.000 ^{+0.012} _{-0.000}	0.375 ^{+0.011} _{-0.017}
Hyades	369	0.424	0.209 ^{+0.054} _{-0.077}	0.421 ^{+0.044} _{-0.028}
NGC2422	343	0.358	0.000 ^{+0.054} _{-0.000}	0.457 ^{+0.008} _{-0.036}
NGC6281	309	0.546	0.510 ^{+0.020} _{-0.025}	0.316 ^{+0.020} _{-0.016}
NGC0884	300	1.445	1.444 ^{+0.024} _{-0.024}	0.419 ^{+0.019} _{-0.016}
IC4756	299	0.597	0.453 ^{+0.047} _{-0.062}	0.473 ^{+0.043} _{-0.029}
NGC1039	296	0.400	0.000 ^{+0.050} _{-0.000}	0.518 ^{+0.011} _{-0.037}
alphaPer	284	0.736	0.284 ^{+0.110} _{-0.163}	0.778 ^{+0.087} _{-0.052}
NGC2548	284	0.331	0.000 ^{+0.080} _{-0.000}	0.421 ^{+0.006} _{-0.039}
NGC6405	275	0.688	0.578 ^{+0.043} _{-0.054}	0.489 ^{+0.042} _{-0.029}
NGC0869	264	1.423	1.423 ^{+0.026} _{-0.027}	0.424 ^{+0.020} _{-0.017}
IC4725	258	1.088	1.086 ^{+0.022} _{-0.022}	0.356 ^{+0.018} _{-0.015}
NGC2423	255	0.474	0.118 ^{+0.067} _{-0.099}	0.537 ^{+0.042} _{-0.043}
NGC6025	243	0.558	0.534 ^{+0.022} _{-0.023}	0.296 ^{+0.020} _{-0.015}
Blanco1	191	0.265	0.000 ^{+0.014} _{-0.000}	0.422 ^{+0.020} _{-0.023}
NGC6633	190	0.562	0.478 ^{+0.041} _{-0.053}	0.392 ^{+0.041} _{-0.027}
Trumpler10	175	0.428	0.000 ^{+0.029} _{-0.000}	0.636 ^{+0.029} _{-0.040}
NGC7092	174	0.338	0.000 ^{+0.025} _{-0.000}	0.497 ^{+0.023} _{-0.032}
IC2602	173	0.805	0.000 ^{+0.203} _{-0.000}	1.020 ^{+0.018} _{-0.127}
NGC2451	145	0.747	0.000 ^{+0.146} _{-0.000}	0.970 ^{+0.030} _{-0.104}
NGC2323	143	0.637	0.601 ^{+0.034} _{-0.042}	0.357 ^{+0.036} _{-0.024}
NGC0752	141	0.408	0.000 ^{+0.039} _{-0.000}	0.586 ^{+0.028} _{-0.044}
IC2391	134	0.732	0.000 ^{+0.176} _{-0.000}	0.938 ^{+0.024} _{-0.116}
Trumpler02	134	0.848	0.842 ^{+0.030} _{-0.032}	0.339 ^{+0.026} _{-0.021}
NGC2158	132	1.107	1.078 ^{+0.050} _{-0.057}	0.537 ^{+0.049} _{-0.035}
NGC6774	127	0.495	0.339 ^{+0.071} _{-0.115}	0.424 ^{+0.076} _{-0.039}
NGC2547	122	0.729	0.000 ^{+0.088} _{-0.000}	1.028 ^{+0.052} _{-0.086}
ComaBer	109	0.257	0.000 ^{+0.025} _{-0.000}	0.391 ^{+0.024} _{-0.030}
NGC6793	103	0.962	0.961 ^{+0.031} _{-0.031}	0.310 ^{+0.026} _{-0.019}
NGC1901	71	0.407	0.000 ^{+0.086} _{-0.000}	0.554 ^{+0.032} _{-0.068}
NGC2232	70	0.681	0.000 ^{+0.121} _{-0.000}	0.967 ^{+0.064} _{-0.108}
Coll140	63	0.647	0.000 ^{+0.109} _{-0.000}	0.956 ^{+0.072} _{-0.105}
NGC3228	60	0.469	0.000 ^{+0.137} _{-0.000}	0.616 ^{+0.032} _{-0.095}
IC4665	56	0.691	0.666 ^{+0.052} _{-0.068}	0.354 ^{+0.062} _{-0.034}